Volume 13
Number 17
7 September 2025
Pages 4567-4848

Biomaterials Science

rsc.li/biomaterials-science

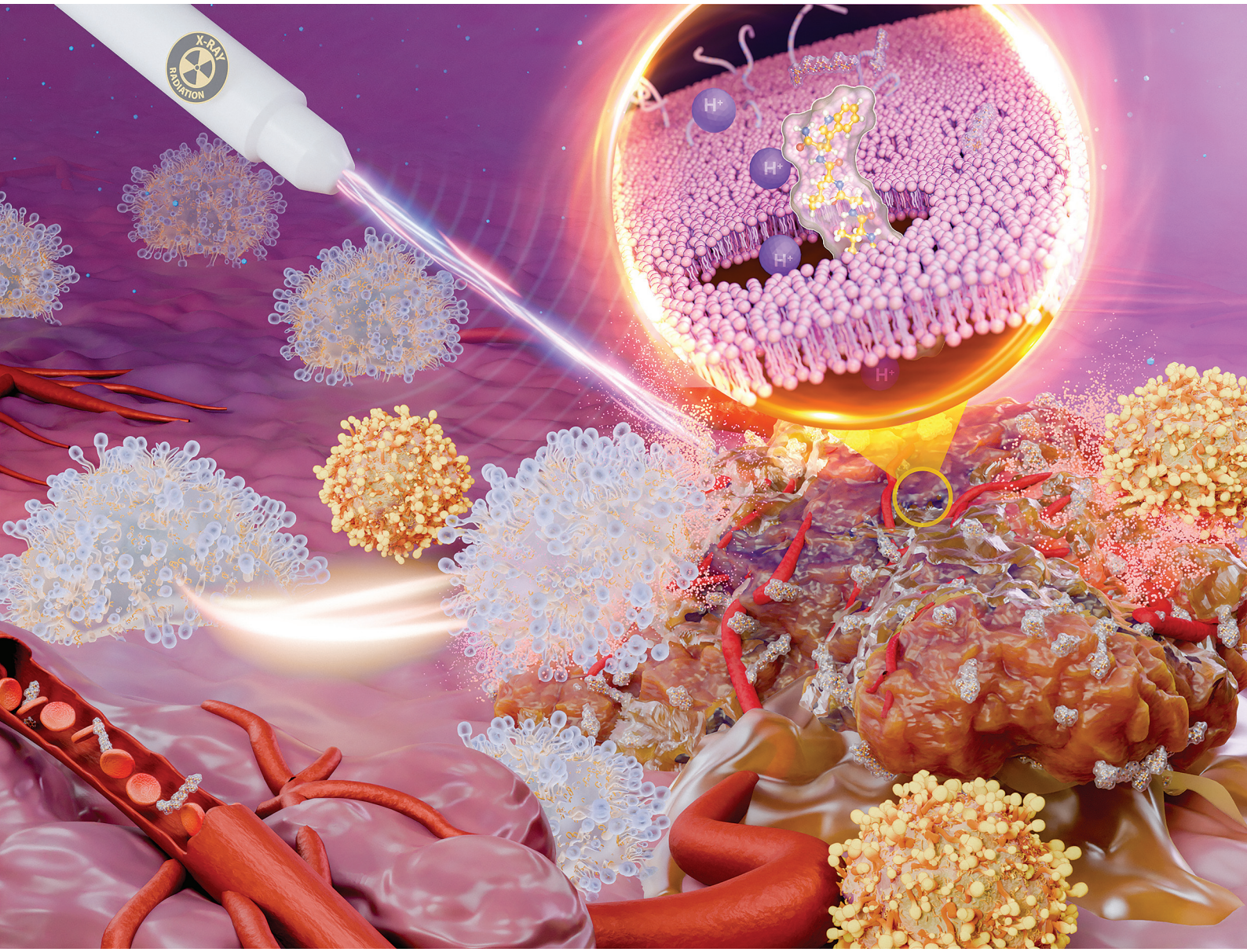

ISSN 2047-4849

ROYAL SOCIETY OF CHEMISTRY

PAPER

Anand Srivastava, Rituparna Sinha Roy *et al.*
Designed gramicidin-inspired stabilized peptide-based therapeutics to potentiate immunotherapy against aggressive kidney cancer

ESB European Society for Biomaterials

Biomaterials Science

ROYAL SOCIETY OF CHEMISTRY

PAPER

View Article Online
View Journal | View Issue

Cite this: *Biomater. Sci.*, 2025, **13**, 4681

Designed gramicidin-inspired stabilized peptide-based therapeutics to potentiate immunotherapy against aggressive kidney cancer†

Argha Mario Mallick, [a] Ananya Chatterjee, [a] Arun Bahadur Gurung, [a] Prithviraj Uttarasili, [b] Archana Tripathi, [a] Monjuri Hembram, [a] Anand Srivastava *[b] and Rituparna Sinha Roy *[a,c,d]

This study reports engineered protease-stable, gramicidin-inspired, peptide-based proton transporter LD8Δ, with alternating L- and D-amino acid residues, to treat the highly chemoresistant, radioresistant, immunosuppressive metastatic renal cell carcinoma (RCC) cell line SK-RC-45. Exploiting the potential of the LD8Δ proton transporter, this study proposes mechanistically rational combination therapy with high translational potential. Current treatment methods involve multi-targeted tyrosine kinase inhibitors, which are accompanied by serious side-effects and exhibit an alarmingly low median overall survival. Computational and experimental data suggested that LD8Δ induced considerable membrane deformation, which supported the destabilization of the intracellular pH regulating mechanism observed in LD8Δ-treated RCC. This mechanistically rational combination therapy using LD8Δ and HIF-2α silencing siRNA induced mitochondrial depolarization, cell cycle arrest, apoptosis, reduction in angiogenesis and disruption of the major oncogenic signalling pathways in SK-RC-45 cells. The designed therapy upregulated the VHL tumour suppressor protein and downregulated HIF-2α protein expression, thus decreasing the activity of the HIF transcriptional factor, which is the master regulator causing clear cell RCC. Additionally, it upregulated DAB2IP and facilitated radiosensitization in the radioresistant SK-RC-45 cells. To the best of our knowledge, this is the first study demonstrating that a designed biocompatible proton transporter can potentiate immunotherapy against RCC by inducing the downregulation of the dual checkpoint proteins CD47, PD-L1 and ganglioside GM2, resulting in enhanced phagocytosis and preventing T cell inactivation and T cell apoptosis.

Received 21st January 2025,
Accepted 13th May 2025

DOI: 10.1039/d5bm00109a

rsc.li/biomaterials-science

1. Introduction

Kidney cancer has seen a significant rise in prevalence, reporting approximately 400 000 new cases and nearly 175 000 deaths worldwide annually, with higher mortality rates in countries with low to moderate income levels.[1] Studies suggest that exposure to air pollution and heavy metals elevates the risk of developing kidney cancer.[2,3] Projections indicate that rise in the occurrence of kidney cancer will continue over the next decade, thus underscoring the pressing need to confront this major global health issue.[1] Renal cell carcinoma (RCC) originates in the renal epithelium and is responsible for more than 90% of incidences of kidney cancer.[4] Furthermore, RCC is highly chemoresistant, radioresistant, and immune-suppressive owing to its highly aggressive angiogenic nature and complex microenvironment, which provide numerous opportunities for immune suppression, making RCC undetectable until advanced stages.[5–8] RCC has been infamous throughout history for its very poor prognosis, with only 8% of individuals diagnosed with metastatic RCC showing 5-year survival rates.[9] Current treatment methods for patients with RCC extensively includes multi-targeted, FDA approved, tyrosine kinase inhibitors, such as sorafenib, sunitinib and pazopanib, which are orally administered and mainly block the activity of platelet-derived growth factor receptor (PDGFR) and vascular endothelial growth factor receptor (VEGFR).[7,9] Other common FDA approved drugs including temsirolimus and immunotherapeutic drugs, such as bevacizumab and nivolumab, are also unable to show promising results.[9] These expensive treatments are also accompanied by side effects including hypertension,

[a]*Department of Biological Sciences, Indian Institute of Science Education and Research Kolkata, Mohanpur-741246, India. E-mail: rituparna@iiserkol.ac.in*
[b]*Molecular Biophysics Unit, Indian Institute of Science, Bangalore, Karnataka 560012, India. E-mail: anand@iisc.ac.in*
[c]*Centre for Advanced Functional Materials, Indian Institute of Science Education and Research Kolkata, Mohanpur-741246, India*
[d]*Centre for Climate and Environmental Studies, Indian Institute of Science Education and Research Kolkata, Mohanpur-741246, India*
† Electronic supplementary information (ESI) available. See DOI: https://doi.org/10.1039/d5bm00109a

nausea, fatigue, impaired wound healing, gastrointestinal perforation, hypothyroidism, various pulmonary issues and alarmingly low median overall survival.[9–12]

Clear cell renal cell carcinoma (ccRCC) is the most common histological subtype of renal cell carcinoma (RCC), constituting approximately 70% of RCC cases in adults.[13,14] The majority of cases of spontaneous ccRCC arises owing to non-functional VHL (von Hippel–Lindau) protein, leading to the constitutive activation of hypoxia inducing factor (HIF).[15] The HIF transcription factor is a heterodimer of HIF-α (oxygen sensing subunits) and HIF-β subunits and regulates the transcription of around 200 genes and is the master regulator for causing ccRCC.[15] HIF-1α regulates the optimum intracellular pH for cancer cell proliferation and HIF-2α promotes cell cycle progression, radioresistance, angiogenesis, and is also responsible for immunosuppression in RCC by downregulating transmembrane glycoproteins such as CD47 and PD-L1, resulting in reduced phagocytosis and T cell activity in ccRCC.[16–18] Small-molecule-based HIF-2α inhibitors have demonstrated effectiveness against RCC but they tend to develop acquired resistance and are associated with serious side effects.[19,20]

Ion channels, specially Ca^{2+} ion channels and K^{+} ion channels, play significant role in immune cell activation and immune cell-mediated cancer cell killing.[21] Modulation of these ion channels particularly in the case of an immunocompromised cancer type, such as RCC, may yield promising results. Interestingly, gramicidin has been successful in inducing cell death in RCC cell lines under *in vitro* conditions.[22,23] Unfortunately, to date, gramicidin has not been established as an anti-cancer drug due to its high haemolytic nature.[24,25] Even combination therapy, the cornerstone of cancer care,[26] has also failed to provide a satisfactory result for patients with metastatic RCC.[27] Most of the attempted combination therapies have yielded either non-tolerable toxicities or very limited additional therapeutic advantages.[27] For example, the combination of sunitinib with an mTOR inhibitor resulted in severe toxicity issues and the combination of bevacizumab with mTOR inhibitors did not prolong the median progression-free survival compared to monotherapy.[28]

Thus, to address the above-mentioned issues, we engineered a gramicidin A (gA)-inspired peptide-based proton transporter, LD8Δ, to induce cell death by disrupting the intracellular pH regulating mechanism mediated by HIF-1α. We also silenced HIF-2α to downregulate multiple oncogenic pathways responsible for causing ccRCC. We examined the efficacy of mechanistically inspired combination therapy having LD8Δ and HIF-2α silencing siRNA in a ccRCC cell line and evaluated the anti-cancer properties of this combination therapy through mitochondrial depolarization, cell cycle arrest, apoptosis and prevention of angiogenesis. Additionally, we also examined the radiosensitization ability and immune-activation properties such as increased phagocytosis and prevention of T cell inactivation and apoptosis of our designed therapy in a metastatic ccRCC cell line, SK-RC-45. We further evaluated the anti-cancer efficacy of our designed combination therapy in an *in vivo* zebrafish model.

2. Results and discussion

2.1. Peptide design

Herein, we aimed to engineer a gA-inspired protease stable, peptide-based proton transporter having effective membrane-deforming ability. Additionally, this transporter needs to be biocompatible and have effective anti-cancer efficacy. gA, composed of alternating L- and D-amino acids in its sequence (Table 1), forms a head-to-head, pore-forming, membrane-spanning β-helix dimer conformation and has demonstrated a significant anti-cancer efficacy against hard-to-treat cancer cell lines and cancer stem cells.[22,25,29,30] However, the haemolytic activity of gA has restricted its use as an anti-cancer drug.[24,25] We deigned the gA-inspired LD8Δ peptide, having alternate L- and D-amino acid residues (Table 1), and evaluated its anti-cancer effectivity against RCC. The presence of alternating D-amino acids endowed the LD8Δ peptide with stability against protease, and thus potential for systemic delivery. Fig. 1a schematically depicts the structure of LD8Δ. The mass of LD8Δ was examined by MALDI-TOF and ESI-MS (Fig. S1†). Fig. S2† depicts the scheme for the synthesis of the peptides by the Fmoc solid-phase peptide synthesis method.

2.2. Mechanistically inspired rational design of combination therapy

The hypoxia-inducible factor (HIF) signaling pathway is fundamentally important in driving the development and progression of ccRCC.[18,32] Between the two main isoforms of HIF-α (HIF-1α and HIF-2α), the HIF-2α isoform acts as a master regulator for causing ccRCC and increases the expression of angiogenic genes, promotes cell cycle progression, EMT (epithelial mesenchymal transition), cancer cell invasion and

Table 1 List of peptides used in this study

Peptide	Sequence	Comments
gA	HCO-Val-Gly-Ala-^{D}Leu-Ala-^{D}Val-Val-^{D}Val-Trp-^{D}Leu-Trp-^{D}Leu-Trp-^{D}Leu-Trp-NHCH$_2$CH$_2$OH	Exhibited high anticancer activity against hard-to-treat cancer cells. Cannot be used as anti-cancer drug due to high haemolytic properties.
LD8Δ	H-Ala-^{D}Val-Leu-^{D}Ala-Val-^{D}Ala-Leu-^{D}Trp-NH$_2$	Peptide used in this study. Protease-stable, non-haemolytic and non-toxic to normal human cells. Can potentiate immuno-combination therapy against the radioresistant metastatic ccRCC SK-RC-45 cell line.
AB36 [31]	PEG9-Arg-C$^{\alpha}$-Octylgly-Arg-Sar-Arg-Gly-Arg-Lys-N$^{\varepsilon}$(D-alpha-tocopherol succinyl)-Arg-Sar-Arg-NH$_2$	Improved transfection reagent with long-term high gene silencing efficacy.

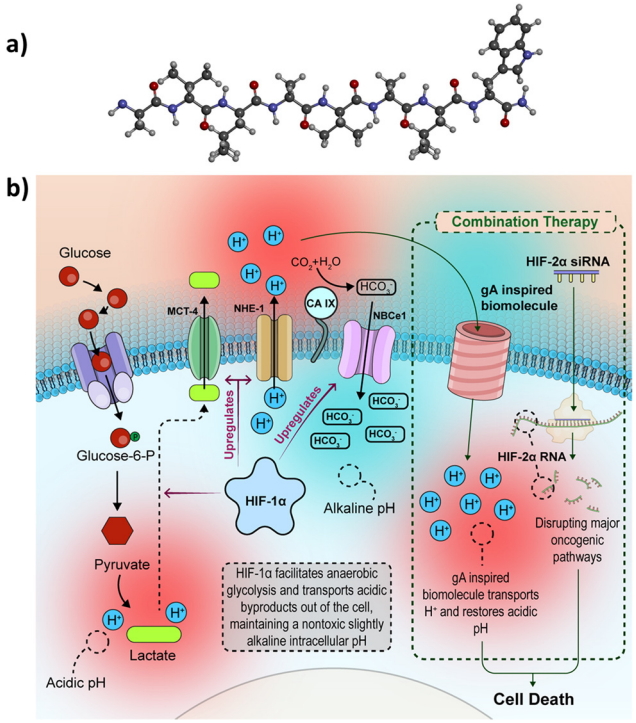

Fig. 1 (a) Schematic of a ball-and-stick model of the LD8Δ peptide. (b) Schematic explaining the development of mechanistically inspired rational combination therapy involving HIF-2α silencing and disrupting pH regulatory machinery of cancer cells using gA-inspired peptide-based proton transporter. Left panel of the diagram is drawn based on the information given in Fig. 3 of ref. 16.

facilitates immune evasion.[18] Small molecule-based HIF-2α antagonists such as PT2399 and PT2385 have exhibited an inhibitory effect against RCC in pre-clinical and phase I clinical studies but both of these small molecules develop acquired resistance and PT2385 causes reduction in RBC precursors by reducing erythropoietin.[19,20] Thus, to address these issues, in this study, we downregulated HIF-2α by RNA interference technology to concomitantly affect all the ccRCC stimulative oncogenic pathways and minimize the undesirable side-effects.[33]

Interestingly, HIF-1α (another isoform of HIF-α), having major tumor suppressor functions in ccRCC,[18] also plays a crucial role in RCC progression. HIF-1α signalling elevates oxygen-independent glycolysis to provide energy to cancer cells and lowers the intracellular pH by acidic metabolite lactate accumulation in the intracellular space of cancer cells.[16,18] According to Volker H. Haase and McIntyre *et al.*, these toxic acidic metabolites can induce apoptosis of cancer cells by lowering the intracellular pH.[16,17] They suggested that HIF-1α upregulates the MCT-4 (monocarboxylic acid transporter 4) and NHE-1 (Na^+/H^+ exchanger 1) proteins, which actively pump out lactate and H^+ ions, respectively, from the intracellular space to the extracellular space, thus preventing the intracellular pH from becoming acidic, which is crucial for cancer cell survival.[16,17] Moreover, HIF-1α also upregulates many pH regulating proteins, such as CA9 (carbonic anhydrase 9) and CA12 (carbonic anhydrase 12), which generate bicarbonate ions in the extracellular space.[17] These bicarbonate ions are further imported to the intracellular space to further increase the intracellular pH (slightly alkaline) of cancer cells.[16] All these collective phenomena give rise to a slightly alkaline intracellular pH and acidic extracellular pH and aid in cancer progression.[17] An acidic extracellular pH favours extracellular matrix degradation, resulting in the invasion and metastasis of cancer.[17]

In this study, we hypothesized that disrupting this pH regulatory machinery can be of high therapeutic importance to treat ccRCC. Thus, to address this issue, we propose that the use of gA-inspired peptide-based H^+ transporters can be effective. Gramicidin ion channels passively transport only monovalent cations with the highest affinity for H^+ ions.[34,35] We hypothesize that gramicidin-inspired peptide-based biomolecules can induce cell death and apoptosis in ccRCC cells by lowering the intracellular pH due to the permeation of H^+ ions from the extracellular space. The combination of HIF-2α gene silencing and biocompatible, ionophore mimicking peptide-based biomolecules can be of high therapeutic importance for treating ccRCC. A schematic diagram explaining the development of mechanistically inspired rational combination therapy is depicted in Fig. 1b.

2.3. Cell viability assessment and evaluation of drug combination interaction

Cell viability was investigated using the MTT assay to test the toxicity of gA and LD8Δ at 24 h, 48 h and 72 h time points against the metastatic ccRCC cell line SK-RC-45 (Fig. 2a and b). The IC_{50} values of gA and LD8Δ at 72 h time point against the SK-RC-45 cell line were calculated to be 992 nM and 27.95 μM using the CompuSyn software[36] based on the MTT assay data (Fig. 2a and b), respectively. The cell viability of combination therapy involving HIF-2α silencing with gA and LD8Δ separately was evaluated at the 72 h (Fig. 2c–f). The 72 h time point was chosen for combination therapy given that lipopeptide AB36 (Table 1) exhibited high transfection efficacy at this time point[31] and LD8Δ exhibited significant toxicity only at the 72 h time point. 25 nM of HIF-2α silencing siRNA was used together with 1.25 μM lipopeptide AB36 at a molar ratio of 50 (peptide : siRNA),[31] and this dose was kept fixed in the combination therapy. Lipopeptide AB36 was selected as the transfection reagent due to its non-toxic nature and its high gene-silencing efficacy, which is comparable to that of the commercial transfection reagent HiPerFect (Qiagen).[31] Moreover, lipopeptide AB36 exhibited better long-term gene silencing efficacy compared to HiPerFect (Qiagen).[31] HIF-2α silencing as monotherapy did not exhibit any significant toxicity in 2D cell culture (Fig. 2c). The combination index (CI) for the combination of HIF-2α silencing with gA or LD8Δ was determined by the Chou–Talalay method[37] using the CompuSyn software,[36] where CI < 1 indicates synergistic interactions, CI = 1 indicates an additive effect and CI > 1 indicates antagonistic interactions. Previous studies by our group

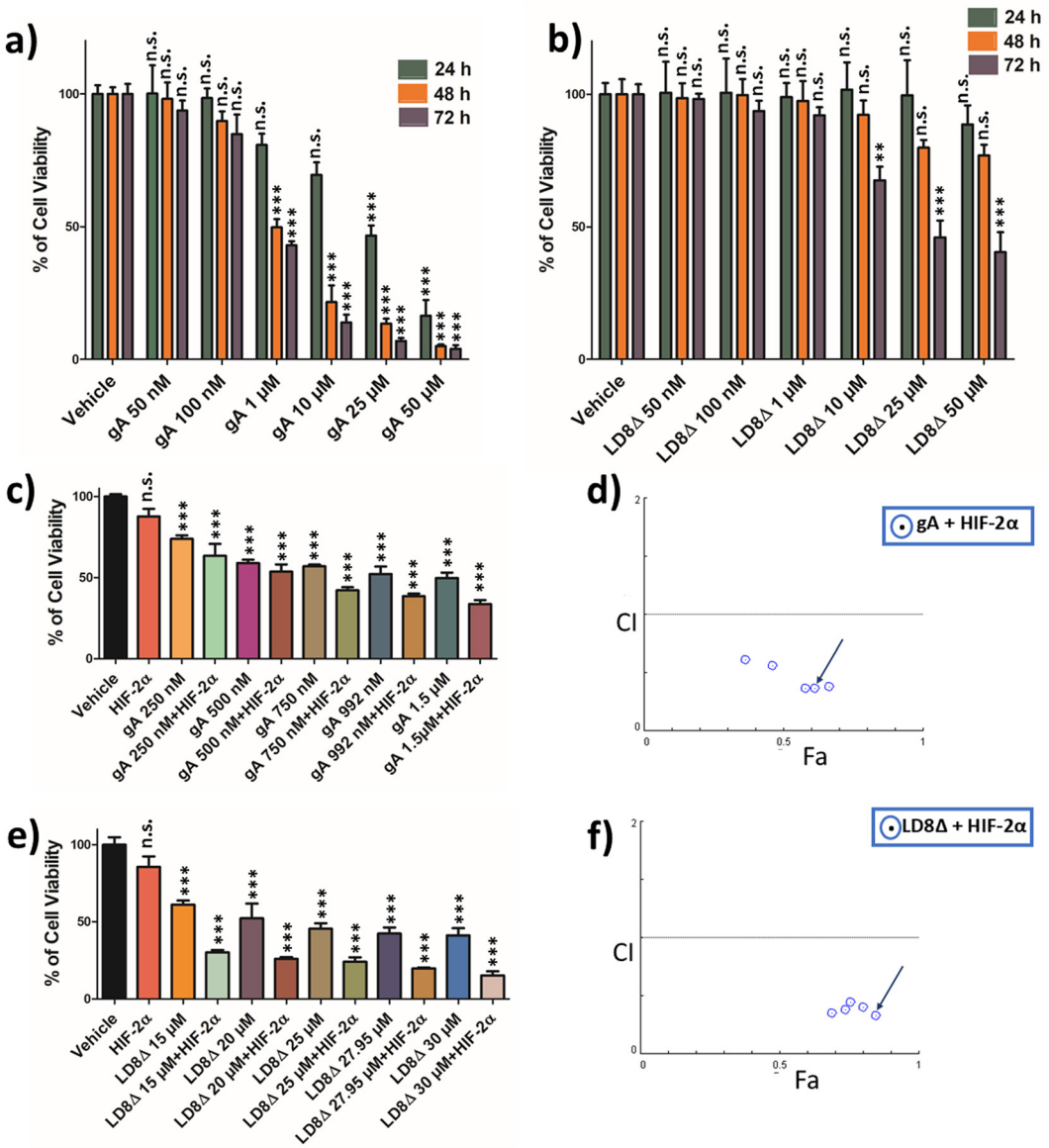

Fig. 2 Cytotoxicity analysis of (a) gramicidin A (gA) and (b) LD8Δ at 24 h, 48 h and 72 h time points in the SK-RC-45 kidney cancer cell line. IC_{50} value of gA and LD8Δ at 72 h was calculated to be 992 nM and 27.95 μM, respectively, using the CompuSyn software, based on the MTT assay data. (c) Cytotoxicity analysis of the combination of gA and HIF-2α gene silencing at 72 h time point in the SK-RC-45 RCC cell line. (d) CI *vs.* Fa (effect) plot at a non-fixed ratio of the combination of gA and HIF-2α gene silencing at 72 h time point in the SK-RC-45 RCC cell line. (e) Cytotoxicity analysis of the combination of LD8Δ peptide and HIF-2α silencing at 72 h time point in the SK-RC-45 kidney cancer cell line. (f) Combination index (CI) *vs.* effect (Fa) plot at a non-fixed ratio of the combination of LD8Δ and HIF-2α gene silencing at 72 h time point in the SK-RC-45 RCC cell line. Selected doses of combination for further experiments are marked using blue arrows (d and f). *p* values are based on one-way ANOVA with Bonferroni post-test (*, $p < 0.05$; **, $p < 0.01$; ***, $p < 0.001$; n.s., not significant compared with respective time point of vehicle in (a) and (b) and vehicle in (c) and (e)). Results are presented as mean ± SEM. Combination therapy of LD8Δ peptide and HIF-2α gene silencing exhibited stronger synergistic effect and stronger cytotoxic ability against SK-RC-45 cells compared with the combination therapy of gA and HIF-2α gene silencing (Table 2).

demonstrated that the dose of 25 nM of siRNA exhibited high transfection efficacy.[31,38] In the presence of 25 nM of siRNA, the SK-RC-45 ccRCC cell line showed around 12% cell death (Fig. 2c), and hence gA and LD8Δ were considered stronger cytotoxic drug compared to 25 nM HIF-2α gene silencing. Thus, the combination studies were performed with non-fixed ratios[39] with doses of gA and LD8Δ near the IC_{50} value and the dose of siRNA was kept fixed at 25 nM. Fig. 2d and f depicts CI *vs.* Fa (effect is abbreviated as "Fa").

All the doses of both gA and LD8Δ used in this study exhibited synergistic interactions with most of the doses exhibiting strong synergistic interaction (CI = 0.3–0.7),[39] and hence effective for combination therapy (Fig. 2d and f) and (Table 2). Interestingly, the combination of LD8Δ with HIF-2α gene silen-

Table 2 Effect (Fa) and combination index (CI) values of different combinations of drugs. Selected combination therapies are marked in bold. The first three rows depict the effect of monotherapy in the presence of three drugs (25 nM HIF-2α silencing siRNA, 992 nM gA and 30 μM LD8Δ)

S. no.	Drug 1 and dose	Drug 2 and dose	Effect (Fa)	CI
1.	HIF-2α silencing siRNA; 25 nM	—	0.12	NA
2.	gA 992 nM	—	0.48	NA
3.	LD8Δ 30 μM	—	0.59	NA
4.	HIF-2α silencing siRNA; 25 nM	gA; 250 nM	0.365	0.61
5.	HIF-2α silencing siRNA; 25 nM	gA; 500 nM	0.46	0.56
6.	HIF-2α silencing siRNA; 25 nM	gA; 750 nM	0.58	0.36
7.	**HIF-2α silencing siRNA; 25 nM**	**gA; 992 nM**	**0.614**	**0.37**
8.	HIF-2α silencing siRNA; 25 nM	gA; 1.5 μM	0.66	0.38
9.	HIF-2α silencing siRNA; 25 nM	LD8Δ; 15 μM	0.69	0.35
10.	HIF-2α silencing siRNA; 25 nM	LD8Δ; 20 μM	0.74	0.38
11.	HIF-2α silencing siRNA; 25 nM	LD8Δ; 25 μM	0.76	0.44
12.	HIF-2α silencing siRNA; 25 nM	LD8Δ; 27.95 μM	0.8	0.4
13.	**HIF-2α silencing siRNA; 25 nM**	**LD8Δ; 30 μM**	**0.85**	**0.33**

cing exhibited higher cytotoxicity and synergism compared to the combination of gA with HIF-2α gene silencing. The best-performing synergistic doses were chosen based on two parameters, *i.e.*, higher effect (Fa) and lower combination index (CI) values. A dose of 992 nM was chosen for gA for combination therapy with HIF-2α silencing having FA of 0.61 and CI of 0.37 (Fig. 2c and d) (Table 2) and 30 μM was chosen for LD8Δ for combination therapy with HIF-2α silencing having FA of 0.85 and CI of 0.33 (Fig. 2e and f) (Table 2) for all further combination studies.

The cytotoxicity of gA and LD8Δ was also checked for non-cancerous human cell lines including human fibroblast cells and HEK-293 (human embryonic kidney 293) cell line. LD8Δ was non-toxic to the non-cancerous HEK-293 cell line and human fibroblast cell line up to 50 μM, whereas gA exhibited significant toxicity to these cell lines at 992 nM (Fig. S3†). Although gA exhibited a very low IC_{50} value compared to LD8Δ in the SK-RC-45 cell line, LD8Δ was non-toxic to non-cancer human cells and exhibited a higher synergistic effect in combination therapy with HIF-2α gene silencing compared to combination with gA against the SK-RC-45 cell line.

2.4. Haemolytic ability of gA and LD8Δ

We examined the haemolytic property of both gA and LD8Δ in goat RBC at the 1 h time point. As reported by other workers,[24,25] we also observed considerable haemolysis of goat RBC in the presence of gA. gA at 992 nM (IC_{50} value for SK-RC-45 at 72 h) exhibited 23.2% ± 2.2% haemolysis and 80% ± 0.9% haemolysis occurred in presence of gA at a 2.5 μM dose (Fig. 3a). Despite its excellent anticancer properties against many chemoresistant cancers such as RCC[40] and gastric cancer stem cells,[25] the use of gA has been restricted to only ectopic application due to its haemolytic nature.[24,25] Interestingly, our data showed that the designed gA-mimicking peptide LD8Δ was non-haemolytic to goat RBC up to 100 μM concentration (Fig. 3a). This result is of high therapeutic significance given that LD8Δ has significant translational potential to be administered intravenously as an anti-cancer drug.

2.5. Immunogenicity assay

The immunogenicity of gA and LD8Δ was checked in goat PBMC (peripheral blood mononuclear cells) by the PBMC proliferation assay. Concanavalin A, a T cell mitogen, served as the positive control at a dose of 5 μg mL^{-1} and PBS served as the negative control.[31] LD8Δ did not exhibit any mitogenic activity up to a 50 μM concentration at 72 h to PBMCs, suggesting that LD8Δ is a non-immunogenic and non-toxic drug candidate (Fig. 3b) and will not trigger any abrupt immune responses. Interestingly, gA was cytotoxic to PBMCs at the 72 h time point and reduced the PBMC population (Fig. 3b).

2.6. Serum stability of LD8Δ

Serum stability is important for the systemic delivery of a drug. The use of alternating D-amino acids in LD8Δ prevented its cleavage by endogenous proteases and ensured its stability in the presence of 10% serum up to 72 h, as determined by mass spectrometry studies (Fig. 3c). Thus, the serum stability and non-haemolytic properties of LD8Δ make it an ideal drug candidate for systemic delivery.

2.7. Cell membrane mimetic GUV poration assay

The GUV poration assay was performed to examine the membrane permeability property of gA and LD8Δ. To investigate this phenomenon, we synthesised plasma membrane mimetic giant unilamellar vesicles (GUVs) comprised of phosphatidylcholine (PC) : cholesterol : phosphatidylethanolamine (PE) at a 65 : 20 : 15 ratio by the gel swelling method (Fig. 3d).[31,41] The lipids were labelled with CM-Dil stain (red color). GUVs were formed in buffer containing FAM (5(6)-carboxyfluorescein, green colour). Confocal microscopy with optical sectioning allowed us to visualize the dark background within the GUVs amidst the green coloured buffer. An intact GUV with no pores or leakage will have a dark interior but the introduction of pores or leakage in the GUV will allow the surrounding green-coloured buffer to leak into the GUV interior, making its interior green. We observed well-formed GUVs with a red exterior and dark interior in untreated GUVs (Fig. 3d). The incubation of GUVs with gA at 992 nM (IC_{50} dose) for 1 h at 37 °C caused leakage in the GUVs. LD8Δ also induced leakage to GUVs at 27.95 μM (IC_{50} dose) after 1 h at 37 °C (Fig. 3d). Interestingly, in addition to the leakage of GUVs, LD8Δ also caused some GUVs to deform from their original spherical shape without fully disrupting the GUVs (Fig. S4†). Melittin (5 μM), a well-known membrane-active pore-forming peptide derived from bee venom, was used as a positive control, which also introduced pores in the GUVs (Fig. 3d). Thus, the GUV poration assay confirmed that similar to gA and melittin, LD8Δ can also induce pores in plasma membrane mimetic GUVs.

2.8. Computational simulation studies for calculation of membrane properties

Here, we examined the changes in cancer cell mimicking membrane induced by LD8Δ, taking melittin as the positive

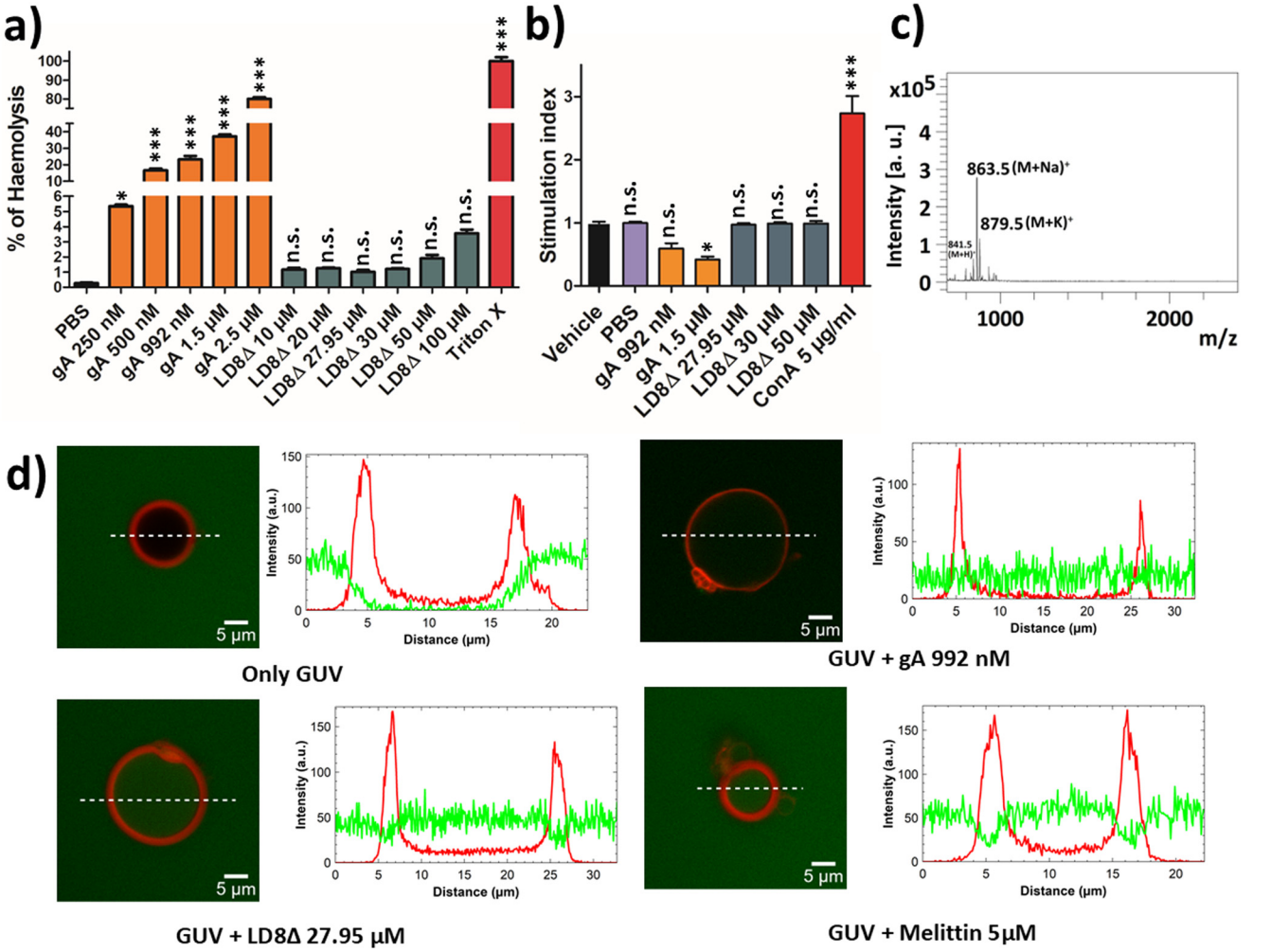

Fig. 3 (a) Percentage of haemolysis induced by gA and LD8Δ peptide in goat blood at 1 h time point. Triton X was taken as the positive control. gA is haemolytic, whereas LD8Δ is non-haemolytic. (b) Graphical depiction of the immunogenicity investigation, determining the stimulation index of PBMCs separated from goat blood *via* MTT experiments. LD8Δ was non-immunogenic up to 72 h, while gA was toxic to PBMCs at higher concentrations. *p* values are based on one-way ANOVA with Bonferroni post-test (*, $p < 0.05$; ***, $p < 0.001$; n.s., not significant compared with PBS in (a) and vehicle in (b)). Results are presented as mean ± SEM. (c) Proteolytic stability of LD8Δ peptide in the presence of 10% FBS at 72 h time point measured using (MALDI-MS) mass spectrometry. This data indicate that the LD8Δ peptide is stable in serum. (d) Representative examples of leakage in the plasma membrane mimicking GUV (dye influx). Confocal images of the plasma membrane mimicking GUV in the presence of 992 nM gA, 27.95 µM LD8Δ peptide and 5 µM melittin are presented in the left panel. Melittin, a 26-residue amphipathic membrane pore forming peptide, was taken as the positive control, and the right panel illustrates the corresponding intensity profiles of FAM dye (green) and CM-DiI dye (red) along the radial axis of GUVs, indicated by the white dotted line.

control, by computational methods. The MD simulations were performed for 300 ns with both peptides aligned parallel to the bilayer-water interface. Both LD8Δ and melittin were completely internalized in the lipid bilayer after 300 ns simulation (Fig. 4a, b and f, g). Interestingly, we observed striking local membrane perturbation specially in the upper leaflet of membrane when LD8Δ was internalized (Fig. 4b). Thus, the changes in membrane properties such as area per lipid, membrane thickness and mean curvature induced by both LD8Δ and melittin were evaluated using the package "FATSLiM".[42]

Area per lipid. The area per lipid (APL) of a membrane is defined by the cross-sectional area along the *X*–*Y* plane of the membrane divided by the total number of lipids present on the membrane leaflet. In both the melittin and LD8Δ peptide systems, the mean local APL value was higher for the region of the membrane where the peptide was located, as shown in (Fig. 4c and h). In addition, the APL plot was shown during the initial, medial, and final periods of the trajectories for both peptide systems (Fig. S5A and Bi–iii†). In the case of the LD8Δ peptide system, the local APL values increased around the peptide location, and the region with higher APL value became broader near the peptide location as the trajectory progressed, as shown in figure (Fig. S5Ai–iii†). Comparing the LD8Δ and melittin systems, the APL values for melittin (0.81–0.84 nm^2) (Fig. S5Bi–iii†) are relatively higher than that for LD8Δ (0.74–0.76 nm^2) (Fig. S5Ai–iii†). The increased APL around both the LD8Δ and melittin peptide systems suggests that the membrane was perturbed to some extent locally.

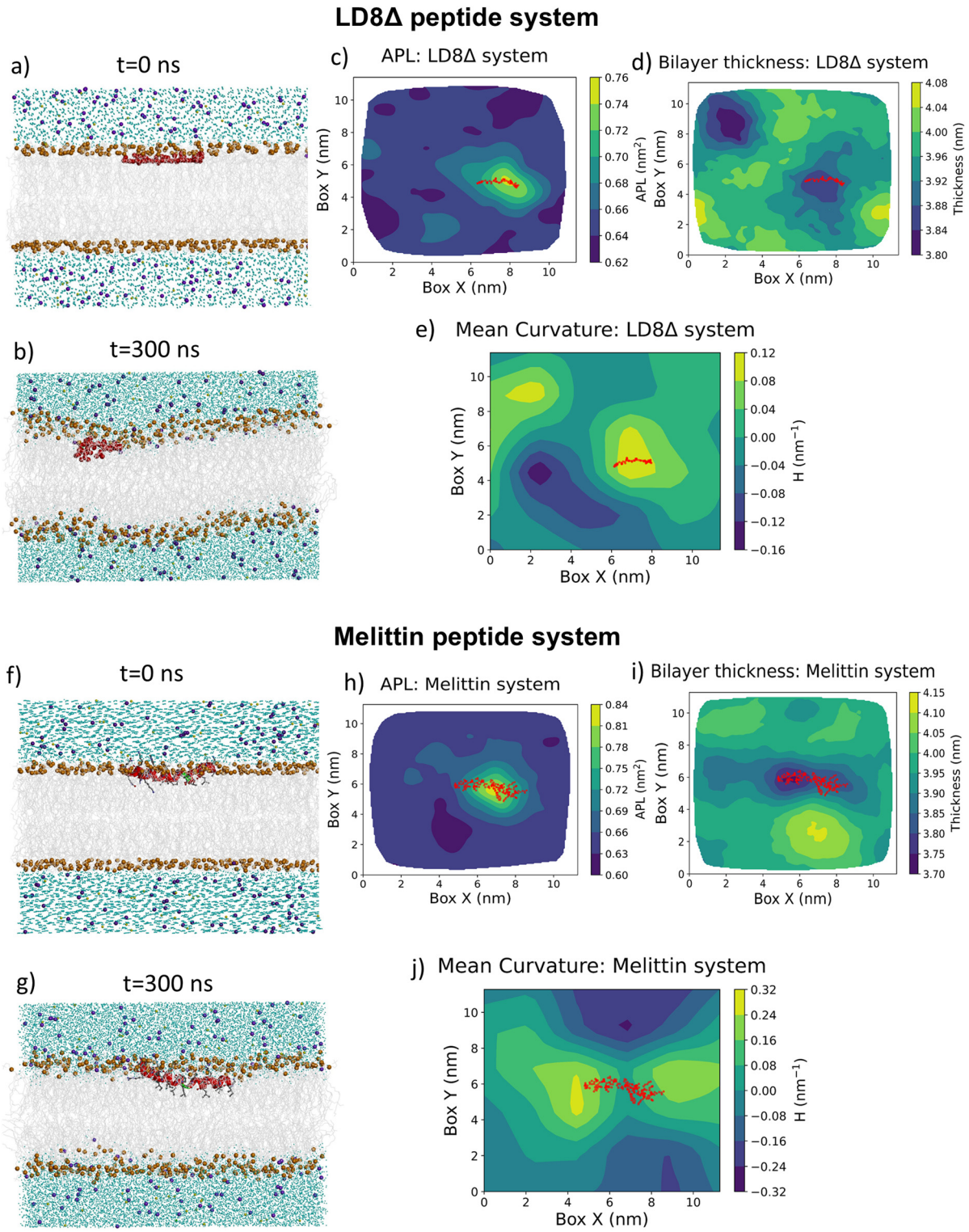

Fig. 4 (a and b) Initial and final binding conformations, respectively, of LD8Δ in the lipid bilayer of the cancer cell mimicking membrane. The LD8Δ peptide is shown in a red ball and stick representation. Membrane properties, such as (c) area per lipid (APL), (d) membrane thickness and (e) mean curvature plots, across the LD8Δ system. (f and g) Initial and final binding conformations, respectively, of melittin in the lipid bilayer of the cancer cell mimicking membrane. Melittin is displayed as red ribbons. (a and b and f and g) Surrounding water molecules are shown as cyan spheres. The phosphate atoms of phospholipids are shown as orange spheres. K^+ and Cl^- ions are shown as purple and yellow spheres, respectively. (h) Area per lipid (APL), (i) membrane thickness and (j) mean curvature plots across the melittin system. The contour plots showing APL, membrane thickness and mean curvature of both LD8Δ and melittin systems are averaged over the trajectory, where *x*-axis and *y*-axis depict box dimension along *X*–*Y* axis, and the color bar depicts the values for the respective membrane properties. For all the plots, the peptide position in the membrane along *X*–*Y* plane is depicted by red dots.

Membrane thickness. The membrane thickness is defined as the distance between the two phosphate planes of the two leaflets of the membrane. There is reduced membrane thickness around the peptide for both peptide systems, as shown in (Fig. 4d and i). In the case of the melittin system, the decrease in the local thickness around the peptide can be noticed from the initial stage of the trajectory, *i.e.* around 3.6 nm, and the trait persisted until the end of the trajectory (Fig. S5Biv–vi†). As the simulation progressed, the region around melittin with a decreased membrane thickness also seemed to widen. In the case of the LD8Δ peptide system, the membrane thickness around the peptide was approximately 4.2–4.0 nm as the simulation progressed; during the final stage of the simulation, the thickness value around the peptide decreased to about 3.8–3.6 nm (Fig. S5Aiv–vi†). Between the two peptides, the decreased thickness is more noticeable in the case of melittin.

Mean curvature. The mean curvature measures the curvature of a surface extrinsically. In this analysis, a value of zero suggests that the surface has no curvature, a negative value refers to a convex surface, and a positive value indicates a concave surface. The plot averaged across the trajectory for both peptide systems shows that there is a positive mean curvature in the vicinity of the peptide, indicating a concave surface (Fig. 4e and j). The LD8Δ peptide system seemed to induce a slightly smaller curvature, *i.e.* ~0.1 nm^{-1}, compared to that of the melittin peptide system, which is 0.2 nm^{-1}. The mean curvature plots at the differential stages for both peptide systems (Fig. S5Avii–ix and S5Bvii–ix†) show that the curvature on the surface manifested gradually as the trajectory progressed, given that the value increased for the LD8Δ peptide system (Fig. S5Avii–ix†). In the initial stages, the mean curvature seems to be ~0.2 nm^{-1}, which increased to 0.75 nm^{-1} in the final stage of trajectory for the LD8Δ peptide system.

The video illustrating the changes in APL, membrane thickness and mean curvature for the last 40 ns of simulation for LD8Δ is provided as **MOV1**, **MOV2** and **MOV3**, and the video illustrating the changes in APL, membrane thickness and mean curvature for the last 40 ns of simulation for melittin is provided as **MOV4**, **MOV5** and **MOV6**, respectively. The membrane properties, *i.e.* APL, membrane thickness and mean curvature, all showed that the LD8Δ peptide has the tendency to perturb the membrane spatial topology. Further, the thickness and the mean curvature results together indicate that LD8Δ deforms the membrane by inducing a concave curvature. In the case of melittin, a higher deformed membrane was observed than the LD8Δ peptide. LD8Δ is a shorter peptide (8 amino acids) compared to melittin (26 amino acids); moreover, in the GUV poration assay (section 2.7), we used around 5-fold higher concentration of LD8Δ compared to melittin, and thus a system with a higher number of LD8Δ peptides interacting with the membrane may induce increased deformation of the membrane.

2.9. Evaluation of mitochondrial depolarization

The ionophore-like activities of the designed biomolecule were evaluated by monitoring Rhodamine 123 (Rh123) dye uptake *via* flow cytometry, which is known as the mitochondrial depolarization assay (reduced Rh123 dye uptake).[22] The H^+ gradient in a polarized mitochondrial membrane is utilized by F_0F_1-ATP synthase for oxidative phosphorylation-dependent ATP synthesis.[43] The mitochondrial membrane depolarization potential of gA and LD8Δ as monotherapy or in combination with HIF-2α gene silencing was checked in the SK-RC-45 metastatic ccRCC cell line. HIF-2α gene silencing, gA 992 nM (IC_{50} dose) and LD8Δ 27.95 μM (IC_{50} dose) exhibited 20.7% ± 1%, 73.3% ± 0.1% and 76.3% ± 0.4% reduction in Rh123 uptake, respectively, in the SK-RC-45 cell line (Fig. 5a). The mitochondrial depolarization indicated that like gA, LD8Δ also permits the transport of H^+ ions. The combination of gA and HIF-2α gene silencing reduced the uptake of Rh123 to 88.6% ± 0.8% and the combination of LD8Δ and HIF-2α gene silencing reduced the uptake of Rh123 to 94% ± 0.1% in the metastatic ccRCC cell line SK-RC-45 (Fig. 5a). The drastic reduction of mitochondrial potential value may eventually lead to cell cycle arrest and reduced viability in ccRCC cell lines, prohibiting the progression of RCC.

2.10. Evaluation of cell cycle arrest

This experiment was performed to examine the reduction in the cell proliferation potential of the designed biomolecules. ccRCC cell lines exhibit a high expression of HIF-2α protein.[18] The cell cycle arresting potential of gA and LD8Δ as monotherapy or in combination with HIF-2α silencing was evaluated by flow cytometry using the propidium iodide (PI) staining method. PI binds with the cellular DNA of dead cells and the DNA content indicates the stage of cell cycle. In the untreated SK-RC-45 cells, 83.4% ± 1.1% cells were in the G0/G1 phase (resting phase or interphase), 8.5% ± 0.9% in the S phase (DNA synthesis phase) and 7.7% ± 0.3% cells in the G2/M phase (gap phase or dividing phase) (Fig. 5b). HIF-2α gene silencing and gA at 992 nM (IC_{50} dose) administration for 72 h arrested SK-RC-45 cells in the G2/M phase with 12.9% ± 0.7% and 14.55% ± 0.1% of cells, respectively (Fig. 5b). The administration of LD8Δ at 27.95 μM (IC_{50} dose) for 72 h induced S and G2/M phase cell cycle arrest, with 17.1% ± 0.3% cells in the S phase and 17.5% ± 0.4% cells in the G2/M phase (Fig. 5b). The combination of gA with HIF-2α silencing at 72 h also induced S and G2/M phase cell cycle arrest, with 13.3% ± 0.3% cells in the S phase and 12.7% ± 0.9% cells in the G2/M phase (Fig. 5b). The combination of LD8Δ with HIF-2α silencing at 72 h induced cell cycle arrest in the SK-RC-45 cell line with 16% ± 1.1% cells in the S phase (Fig. 5b). The individual images of flow cytometry analysis for the cell cycle arrest of the SK-RC-45 cells treated with individual conditions taken in this study are presented in Fig. S6.† Notably, the combination of both gA and LD8Δ with HIF-2α silencing significantly increased the SK-RC-45 cells in the sub G0/G1 phase (Fig. 5b), which suggests that the designed combination therapy may cause DNA fragmentation and induce apoptosis in metastatic ccRCC SK-RC-45 cells.[44]

2.11. Evaluation of apoptosis and necrosis

To evaluate the apoptosis or necrosis induced by gA and LD8Δ as monotherapy or in combination with HIF-2α silencing,

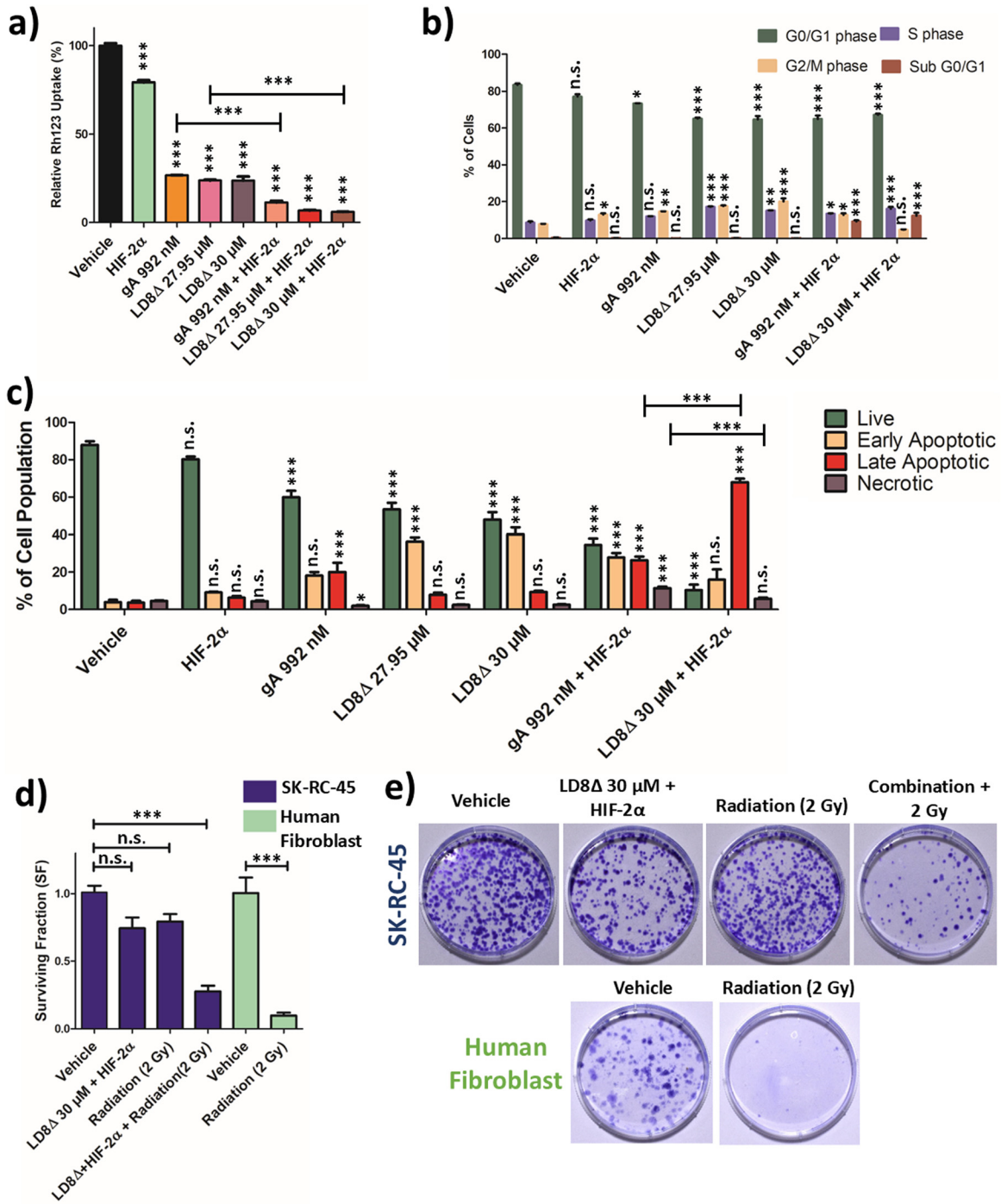

Fig. 5 (a) Mitochondrial transmembrane potential assay performed using flow cytometry revealed decreased rhodamine 123 dye uptake following a 72 h incubation period in the presence of gA, LD8Δ peptide and HIF-2α gene silencing, both in monotherapy and combination therapy in SK-RC-45 kidney cancer cells. (b) Cell cycle analysis of gA, LD8Δ peptide and HIF-2α gene silencing, both in monotherapy and combination therapy in SK-RC-45 kidney cancer cells, 72 h post-treatment by PI staining. (c) Apoptosis and necrosis analysis of SK-RC-45 kidney cancer cells treated with gA, LD8Δ peptide and HIF-2α gene silencing, both in monotherapy and combination therapy, after 72 h post treatment. *p* values are based on one-way ANOVA with Bonferroni post-test (*, $p < 0.05$; **, $p < 0.01$; ***, $p < 0.001$; n.s., not significant compared with vehicle in (a), respective cell cycle phases of vehicle in (b) and respective cell viability states of vehicle in (c)). Results are presented as mean ± SEM. Combination of LD8Δ peptide and HIF-2α gene silencing exhibited more apoptotic cell population and less necrotic cell population compared with the combination of gA and HIF-2α gene silencing. (d) Surviving fraction (SF) of SK-RC-45 cells and non-cancerous human fibroblast cells as obtained from clonogenic assay. *p* values are based on one-way ANOVA with Bonferroni post-test (***, $p < 0.001$; n.s., not significant). Results are presented as mean ± SEM. (e) Representative photographs of clonogenic assay performed in 100 mm Petri dish. Results demonstrated that SK-RC-45 cell line is highly radioresistant and human fibroblast cell line is radiosensitive. Treatment of combination of 30 μM LD8Δ and HIF-2α gene silencing sensitized SK-RC-45 cells to radiotherapy.

Table 3 Percentage of apoptotic and necrotic cell populations post treatment

S. no.	Condition	% of alive cells	% of early apoptotic cells	% of late apoptotic cells	% of necrotic cells
1.	Vehicle	87.96	3.9	3.65	4.5
2.	HIF-2α	80.25	9.1	6.25	4.4
3.	gA 992 nM	59.9	18.1	20.0	1.9
4.	LD8Δ 27.95 μM	53.45	36.3	7.85	2.4
5.	LD8Δ 30 μM	47.9	40.2	9.4	2.5
6.	gA 992 nM + HIF-2α	34.5	27.75	26.4	11.4
7.	LD8Δ 30 μM + HIF-2α	10.35	15.95	67.98	5.7

annexin V/PI-stained SK-RC-45 cells were analysed by flow cytometry. Annexin V binds to phosphatidylserine, which flips to the outer cell membrane leaflet during apoptosis. Counterstaining with PI labels the nucleus of late apoptotic and necrotic cells. Generally, annexin V−/PI− cells are considered live cells, annexin V+/PI− are considered cells in the early apoptotic phase, annexin V+/PI+ as late apoptotic or secondarily necrotic cells and annexin V−/PI+ are considered necrotic cells.[45] The percentage of early apoptosis, late apoptosis and necrosis induced by gA and LD8Δ as monotherapy or in combination with HIF-2α silencing is presented in Table 3 (Fig. 5c). The total apoptosis induced by the combination therapy of gA (992 nM) and HIF-2α silencing on SK-RC-45 cells was 54.1% ± 7.2% (early apoptosis and late apoptosis combined) and 11.4% ± 1.5% of cells were found to be necrotic (Fig. 5c). The total apoptosis induced by the combination therapy of LD8Δ (30 μM) and HIF-2α silencing on SK-RC-45 cells was 83.9% ± 6.3% (early apoptosis and late apoptosis combined) and only 5.7% ± 1.2% of cells exhibited necrosis (Fig. 5c). The individual images of flow cytometry analysis for evaluating apoptosis and necrosis of SK-RC-45 cells treated with individual conditions employed in this study are depicted in Fig. S7.† Interestingly, the combination of LD8Δ (30 μM) and HIF-2α silencing exhibited significantly higher apoptosis and lower necrosis than the combination of gA (992 nM) and HIF-2α silencing on SK-RC-45 cells (Fig. 5c). Apoptosis is advantageous over necrosis given that apoptosis does not elicit any inflammatory pathways, whereas necrosis leads to the uncontrolled release of inflammatory cellular contents.[46] This data demonstrates highly effective therapeutic efficacy of the designed combination therapy of LD8Δ (30 μM) and HIF-2α silencing against the ccRCC SK-RC-45 cell line.

2.12. Assessment of degree of radioresistance of SK-RC-45 cell line and radiosensitization activity in the presence of combination therapy

The clonogenic assay was performed to investigate the degree of radioresistance and clonogenic survival following irradiation of the ccRCC SK-RC-45 cell line.[47] After observing a significant increase in apoptosis in SK-RC-45 cells following treatment with the combination of LD8Δ 30 μM and HIF-2α gene silencing (Fig. 5c), we explored whether this combination could sensitize SK-RC-45 cells to radiotherapy, overcoming the inherent radioresistant nature of RCC.[48] The cells were radiated with a single dose of 2 Gy radiation, where a high SF2 (surviving fraction after 2 Gy radiation) indicates radioresistance.[49] SF2 is regarded as the benchmark dose and is substantiated by robust clinical data and *in vivo* murine model.[49] The SF2 for the ccRCC SK-RC-45 cell line was determined to be 0.79 ± 0.1, indicating that the SK-RC-45 cell line is highly radioresistant (Fig. 5d and e).[49,50] The SF2 for the non-cancerous human fibroblast cell line was determined to be 0.1 ± 0.03, indicating its radiosensitive nature (Fig. 5d and e). The surviving fraction (SF) for SK-RC-45 cells after treatment with the combination of LD8Δ 30 μM and HIF-2α gene silencing for 72 h was 0.74 ± 0.1 (Fig. 5d and e). When the treated SK-RC-45 cells were further irradiated with a 2 Gy dose, the SF was calculated to be 0.28 ± 0.06 (Fig. 5d and e). This significant decrease in SF indicates that the designed combination therapy of 30 μM LD8Δ and HIF-2α gene silencing sensitized the metastatic ccRCC SK-RC-45 cell line to radiation therapy, which can be of high therapeutic value.

2.13. Elucidation of the mechanism of action induced by monotherapy and combination therapy

Evans *et al.* hypothesized that gramicidin induced an alteration in the plasma membrane composition and compression can affect the orientation of different receptors present in the plasma membrane, leading to altered oncogenic signalling pathways.[51] David *et al.* reported that gA downregulated the expression of both the HIF-2α and HIF-1α proteins in RCC cell lines by upregulating the VHL (Von Hippel–Lindau) protein.[52] Downregulation of HIF transcription factors in RCC led to the reduced transcription of various oncogenes, ultimately reducing the growth of human RCC xenografted tumors in an *in vivo* model.[52] Thus, we were interested to check if a similar mode of function is also exhibited by LD8Δ.

2.13.1 Structural insights into mutated VHL (Von Hippel–Lindau) by computational studies. The metastatic ccRCC cell line SK-RC-45 has predominant Arg82Pro mutation in the VHL protein.[53] Alves and group reported that 42.9% of samples had non-mutated VHL among histologically confirmed ccRCC samples.[54] A single point mutation, Arg82Pro,[53] was introduced in native VHL, specific to the SK-RC-45 cell line to generate the mutant VHL-HIF-2α complex computationally (Fig. 6a). MD simulation was performed for 100 ns and the total interaction energy between the VHL (PDB ID: 6BVB, chain V) and HIF-2α (PDB ID: 6BVB, chain H) proteins in the wild-type and mutant complex was calculated (Fig. 6b). The total interaction energy between the wild-type VHL and HIF-2α

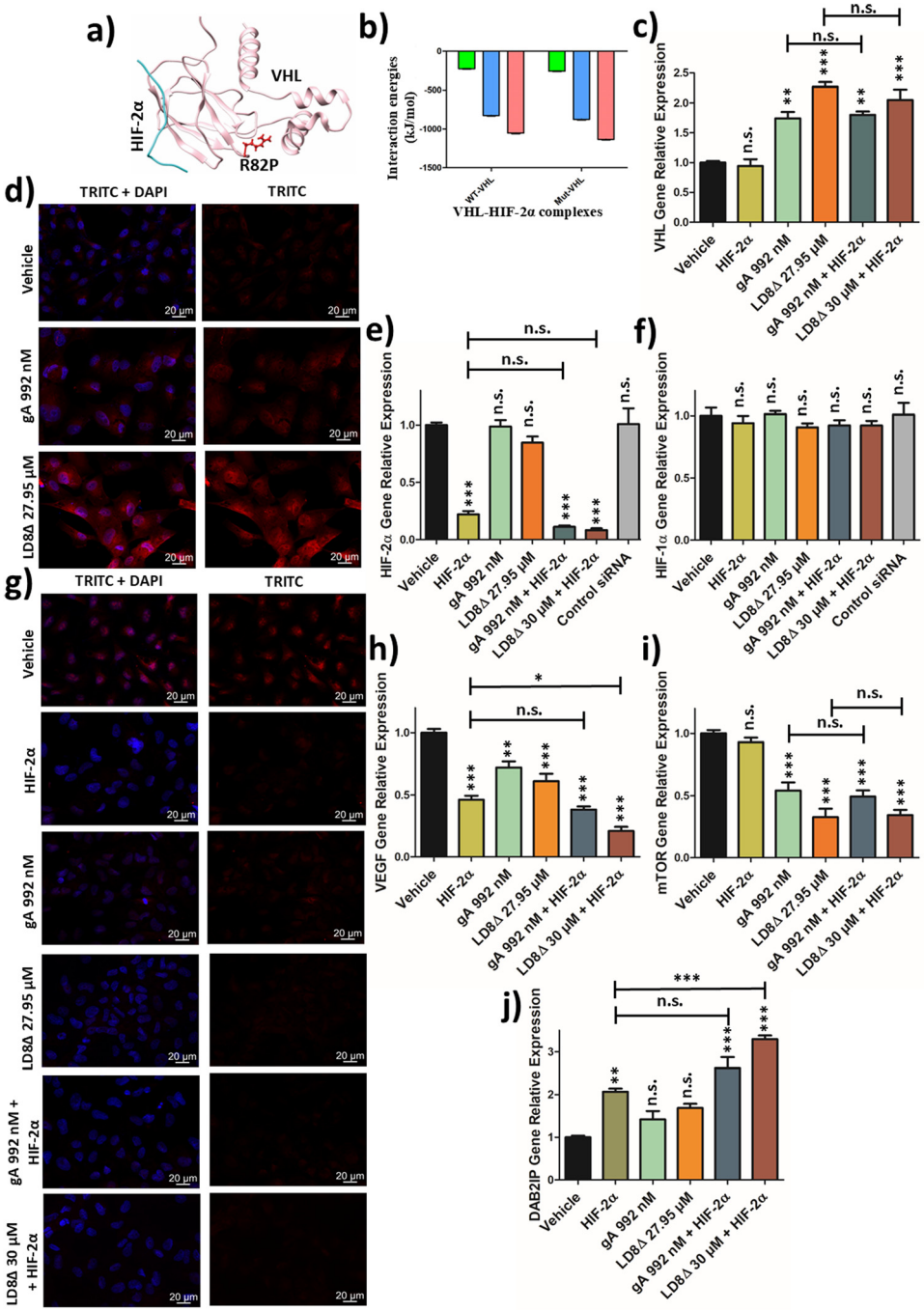

Fig. 6 (a) Crystal structure of the VHL-HIF-2α complex (PDB ID: 6BVB). The Arg82Pro mutation site in VHL protein specific to the SK-RC-45 renal cell carcinoma (RCC) cell line is represented in a red ball and stick model. VHL and HIF-2α proteins are shown in ribbon representation in pink and cyan, respectively. (b) Bar graph showing the average interaction energy of wild-type VHL and mutant VHL with HIF-2α. The total interaction energy (pink) is the sum of van der Waals energy (green) and electrostatic energy (blue). Real-time PCR data showing relative gene expression of (c) VHL (von Hippel–Lindau, responsible for degradation of HIF-α protein), (e) HIF-2α, (f) HIF-1α, (h) VEGF, (i) mTOR and (j) DAB2IP gene in SK-RC-45 cells after treatment with gA, LD8Δ peptide and HIF-2α gene silencing, both in monotherapy and combination therapy at 72 h time point. Immunofluorescence of (d) VHL protein and (g) HIF-2α protein after treatment with gA (992 nM) and LD8Δ peptide (27.95 μM) at 72 h time point compared with untreated SK-RC-45 cells, considered as vehicles. Scale bar = 20 μM. VHL is upregulated at both the gene and protein levels in the presence of both gA and LD8Δ peptide. Both gA and LD8Δ peptide have no influence in downregulating HIF-2α at gene expression level. Both monotherapy and combination therapy did not have any effect in HIF-1α gene expression. Both monotherapy and combination therapy has drastically reduced HIF-2α protein expression. Combination therapy of LD8Δ peptide and HIF-2α gene silencing exhibited significant reduction in VEGF gene expression compared with monotherapy. Both gA and LD8Δ peptide induced significant reduction in mTOR gene expression. Combination therapy of LD8Δ peptide and HIF-2α gene silencing exhibited significant upregulation in DAB2IP gene expression compared with monotherapy. *p* values are based on one-way ANOVA with Bonferroni post-test (*, $p < 0.05$; **, $p < 0.01$; ***, $p < 0.001$; n.s., not significant compared with vehicle). Results are presented as mean ± SEM.

proteins was calculated to be −1053.4 ± 4.3 kJ mol^{-1} (−227.4 ± 1.1 kJ mol^{-1} van der Waals energy and −825.9 ± 3.9 kJ mol^{-1} electrostatic energy) and the total interaction energy between the mutated VHL and HIF-2α proteins was calculated to be −1133.8 ± 4.6 kJ mol^{-1} (−257.9 ± 1.0 kJ mol^{-1} van der Waals energy and −875.9 ± 4.4 kJ mol^{-1} electrostatic energy) (Fig. 6b). The point mutation Arg82Pro in the VHL protein did not significantly affect the binding interaction between VHL and HIF-2α (Fig. 6b). This lack of effect may be due to the position of the Arg82Pro mutation, which is distant from the protein–protein interface in the VHL-HIF-2α complex (Fig. 6a). The limitation of this study is that we could not consider the full-length VHL-HIF-2α complex given that its complete crystal structure is unavailable in the protein data bank.[55] Moreover, due to the complexity of atomistic simulations of multiprotein complexes, we only considered the interaction between the VHL and HIF-2α proteins.

2.13.2 Investigating the gene and protein expression of VHL (Von Hippel–Lindau), HIF-1α and HIF-2α after treatment with monotherapy and combination therapy. Next, we checked the relative expression of VHL, HIF-1α and HIF-2α gene in the SK-RC-45 cell line following 72 h treatment with gA (992 nM, IC_{50} dose), LD8Δ (27.95 μM, IC_{50} dose), silencing HIF-2α gene, combination therapy of gA (992 nM) with HIF-2α silencing and combination of LD8Δ (30 μM) with HIF-2α silencing by real time PCR (Fig. 6c, e, and f). Interestingly, both gA and LD8Δ increased the relative expression of VHL with the relative gene expression of 1.74 ± 0.2 and 2.27 ± 0.1, respectively, compared to the vehicle (Fig. 6c). No significant change in VHL gene expression was observed after HIF-2α silencing both in monotherapy and combination therapy given that VHL functions upstream to HIF-2α in the signalling cascade (Fig. 6c).[18] Immunofluorescence studies also confirmed that there is significant increase in VHL protein expression after the treatment of the SK-RC-45 cell line for 72 h with gA (992 nM, IC_{50} dose) and LD8Δ (27.95 μM, IC_{50} dose) compared to the untreated cells (Fig. 6d). According to Frew *et al.*, the VHL protein exists in two isoforms, with the longer protein isoform mainly localizing in the cytoplasm and the shorter protein isoform mainly localizing in the nucleus.[56] The studies by the groups of Williams[57] and Krek[56] hinted the possibility that the VHL protein isoform localizing in the nucleus is mainly responsible for HIFα repression. The rhodamine intensity from maximum intensity projection (MIP) image in the nucleus was calculated to 59.3 ± 3.8 a.u. for the untreated sample, and interestingly after treatment with gA and LD8Δ, the rhodamine intensity from MIP image in the nucleus was calculated to be 92.3 ± 9.5 a.u. and 215.6 ± 35.2 a.u, respectively.

According to these data, we hypothesized that the mutation Arg82Pro in the VHL protein in the SK-RC-45 cell line may not be responsible for the loss of VHL-mediated HIF-2α degradation. According to the gene level and protein level expression of VHL (Fig. 6c and d), it may be possible that the oncogenesis in SK-RC-45 can be due to the low level of VHL protein in the SK-RC-45 cell line. Given that we observed an increase in VHL protein mainly localizing in the nucleus after treatment, we were interested to investigate if it could lead to enhanced degradation of the HIF-2α protein in the SK-RC-45 cell line.

No significant changes in HIF-2α and HIF-1α gene expression were observed after treatment with both gA and LD8Δ (Fig. 6e and f), respectively. Silencing the HIF-2α gene drastically reduced HIF-2α gene expression to 0.22 ± 0.04 (Fig. 6e) but no significant change was observed in the level of HIF-1α gene (Fig. 6f). The combination therapies did not significantly alter the HIF-2α gene expression compared to only HIF-2α gene silencing (Fig. 6e).

Interestingly, both the monotherapies and combination therapies significantly decreased the HIF-2α protein expression, with the combination therapies further lowering the HIF-2α protein expression compared to monotherapy (Fig. 6g). The rhodamine intensity (HIF-2α protein intensity) of SK-RC-45 cells from MIP images for each condition is mentioned in Table 4.

Our findings indicate that gA and LD8Δ induced an increase in the expression of the VHL protein, which reduced HIF-2α protein expression. Interestingly, Rajasekaran and coworkers reported similar findings with gA-treated RCC cell lines.[52]

2.14. Relative expression of VEGF, mTOR and DAB2IP genes relevant to therapeutic implications for ccRCC

The relative gene expression of three highly therapeutically relevant genes were checked post-treatment with monotherapy and combination therapy. Aberrant angiogenesis drives chemoresistance and radioresistance in RCC.[58] Our designed combination therapy of LD8Δ (30 μM) with HIF-2α silencing significantly reduced VEGF transcription (Fig. 6h and Table 5).

Table 4 Mean rhodamine intensity in SK-RC-45 cells calculated using MIP images

Protein investigated	Conditions with dose	Mean rhodamine intensity (a.u.)
HIF-2α (multi oncogenic switch responsible for ccRCC)	Vehicle	41.1 ± 1.6
	HIF-2α	15.9 ± 1.5
	gA 992 nM	20.3 ± 4.4
	LD8Δ 27.95 μM	16.3 ± 1.3
	gA 992 nM + HIF-2α	15.4 ± 2.4
	LD8Δ 30 μM + HIF-2α	9.5 ± 0.3
CD47 (prevents phagocytosis of cancer cells)	Vehicle	45.6 ± 3.6
	HIF-2α	13.1 ± 0.7
	gA 992 nM	17.5 ± 3.4
	LD8Δ 27.95 μM	14.2 ± 1.3
	gA 992 nM + HIF-2α	12.1 ± 0.7
	LD8Δ 30 μM + HIF-2α	9.7 ± 0.4
PD-L1 (prevents T cell activation)	Vehicle	24.1 ± 1.5
	HIF-2α	8.7 ± 0.5
	gA 992 nM	9.98 ± 0.4
	LD8Δ 27.95 μM	8.91 ± 0.2
	gA 992 nM + HIF-2α	7.99 ± 0.1
	LD8Δ 30 μM + HIF-2α	6.2 ± 0.1
GM-2 (responsible for apoptosis of T cells)	Vehicle	89.13 ± 7.6
	HIF-2α	37.84 ± 6.4
	gA 992 nM	19.57 ± 2.0
	LD8Δ 27.95 μM	17.26 ± 0.9
	gA 992 nM + HIF-2α	16.43 ± 3.0
	LD8Δ 30 μM + HIF-2α	11.0 ± 0.7

Table 5 Relative expression of genes relevant to therapeutic implications for ccRCC

mRNA investigated	Conditions with dose	Relative mRNA expression_72 h
VEGF (responsible for angiogenesis)	HIF-2α	0.46 ± 0.05
	gA 992 nM	0.72 ± 0.07
	LD8Δ 27.95 μM	0.61 ± 0.08
	gA 992 nM + HIF-2α	0.38 ± 0.03
	LD8Δ 30 μM + HIF-2α	0.21 ± 0.05
mTOR (responsible for cell proliferation)	HIF-2α	0.93 ± 0.05
	gA 992 nM	0.54 ± 0.09
	LD8Δ 27.95 μM	0.33 ± 0.1
	gA 992 nM + HIF-2α	0.49 ± 0.07
	LD8Δ 30 μM + HIF-2α	0.33 ± 0.1
DAB2IP (responsible for radio-sensitization)	HIF-2α	2.07 ± 0.1
	gA 992 nM	1.42 ± 0.28
	LD8Δ 27.95 μM	1.69 ± 0.13
	gA 992 nM + HIF-2α	2.62 ± 0.36
	LD8Δ 30 μM + HIF-2α	3.3 ± 0.12

Table 6 Relative expression of genes relevant to immunotherapy against ccRCC

mRNA investigated	Conditions with dose	Relative mRNA expression_72 h
CD47 (prevents phagocytosis of cancer cells)	HIF-2α	0.56 ± 0.05
	gA 992 nM	0.7 ± 0.07
	LD8Δ 27.95 μM	0.63 ± 0.08
	gA 992 nM + HIF-2α	0.49 ± 0.06
	LD8Δ 30 μM + HIF-2α	0.24 ± 0.05
PD-L1 (prevents T cell activation)	HIF-2α	0.52 ± 0.14
	gA 992 nM	0.58 ± 0.06
	LD8Δ 27.95 μM	0.61 ± 0.11
	gA 992 nM + HIF-2α	0.31 ± 0.05
	LD8Δ 30 μM + HIF-2α	0.14 ± 0.03
GM2-synthase (responsible for apoptosis of T cells)	HIF-2α	0.83 ± 0.04
	gA 992 nM	0.74 ± 0.07
	LD8Δ 27.95 μM	0.56 ± 0.05
	gA 992 nM + HIF-2α	0.39 ± 0.03
	LD8Δ 30 μM + HIF-2α	0.24 ± 0.04

Mutations in mTOR are common in ccRCC leading to hyperactivation and cancer cell proliferation.[59,60] Alongside HIF-α, VHL also ubiquitinates RAPTOR, a key mTORC1 component.[60] Both gA (992 nM) and LD8Δ (27.95 μM) significantly reduced mTOR gene expression (Fig. 6i and Table 5), while HIF-2α silencing showed no additional effect. LD8Δ suppressed VEGF and mTOR signalling in the metastatic ccRCC SK-RC-45 cell line, which can be beneficial for treating RCC, given that LD8Δ is non-haemolytic, serum-stable and has potential to be used as oral medicine. As demonstrated by Yun *et al.*, the Ras GTPase-activating family protein DAB2IP can degrade PARP-1 (poly(ADP-ribose)polymerase) and elevated level of PARP-1 leads to radioresistance in kidney cancer cells.[61] The relative expression of DAB2IP mRNA exhibited a significant increase in the combination therapy of LD8Δ (30 μM) with HIF-2α silencing (Fig. 6j and Table 5), suggesting that the designed combination therapy can be used to sensitize SK-RC-45 cells to radiotherapy.

2.15. Immunoactivation induced by monotherapy and combination therapy

2.15.1. Relative expression of CD47 and PD-L1 mRNA and protein. The relative m-RNA expression of CD47 and PD-L1 was checked post-treatment to evaluate the reduction in the immunosuppression in ccRCC cells. CD47 is overexpressed in various tumors, and also serve as a bio-marker for malignant cancer cells.[62] CD47 interacts with SIRPα present in macrophages and monocytes, providing the "don't eat me" signal, and thus evading cancer cell phagocytosis by macrophages.[62] PD-L1 is also a transmembrane glycoprotein expressed in cancer cells.[63] The interaction of PD-L1 of cancer cells with the immune checkpoint protein PD-1 of T cells serves as "brakes" and inhibits T cell activation, providing immune evasion to cancer cells.[63] CD47 and PD-L1 were reported to be highly upregulated in ccRCC, leading to poor prognosis.[64,65] HIF activation leads to the upregulated expression of immune evasion genes such as PD-L1 and CD47 in RCC.[18] The values of relative CD47 and PD-L1 gene expression post-treatment with monotherapy and combination therapy are presented in Table 6 and Fig. 7a and b. Interestingly, the designed combination therapy of only LD8Δ (30 μM) with HIF-2α silencing exhibited a significant decrease in both CD47 and PD-L1 gene expression compared to monotherapy by HIF-2α gene silencing (Fig. 7a and b).

Immunostaining of both CD47 and PD-L1 proteins was performed separately to check the protein levels in the SK-RC-45 cell line at the 72 h time point (Fig. 7c and d). The immunofluorescence data indicate that the combination therapies significantly lowered both CD47 and PD-L1 protein expressions compared to monotherapies (Fig. 7c, d and Table 4).

2.15.2. Evaluation of apoptosis of T cells induced by SK-RC-45 cell line. Tannenbaum and co-workers reported that many cancer cells including RCC overexpress death ligands and gangliosides, inducing the apoptosis of around 90% of tumour-infiltrating T cells.[66] In our study, Jurkat cells were co-incubated with the SK-RC-45 cell line for 72 h at a 1 : 3 ratio to mimic the tumour microenvironment and flow cytometry studies were performed to determine the apoptotic cell population of Jurkat cells by annexin V/PI staining.[66] The untreated SK-RC-45 cells induced apoptosis in 87% ± 0.3% of Jurkat cells (Fig. 8a). Monotherapies, including HIF-2α silencing, gA (992 nM), and LD8Δ (27.95 μM), reduced Jurkat cell apoptosis to 70.9% ± 5.2%, 47.5% ± 2.6%, and 38.7% ± 3.5%, respectively (Fig. 8a), indicating that in the presence of these drugs, active T cells can induce a cytotoxic effect on cancer cells. The combination therapy of gA 992 and HIF-2α silencing and combination of LD8Δ 30 μM and HIF-2α silencing exhibited 11.2% ± 0.6% and 9.8% ± 0.4% apoptosis of Jurkat cells, respectively (Fig. 8a), thus nearly completely abrogating the ability of SK-RC-45 cells to induce apoptosis to Jurkat cells. The individual images of the flow cytometry analysis for evaluating the apoptosis of Jurkat cells mediated by SK-RC-45 cells treated with individual conditions taken in this study are depicted in Fig. S8.†

Kudo and co-workers indicated that GM2 ganglioside was primarily responsible for RCC cell-mediated T cell apoptosis.[67]

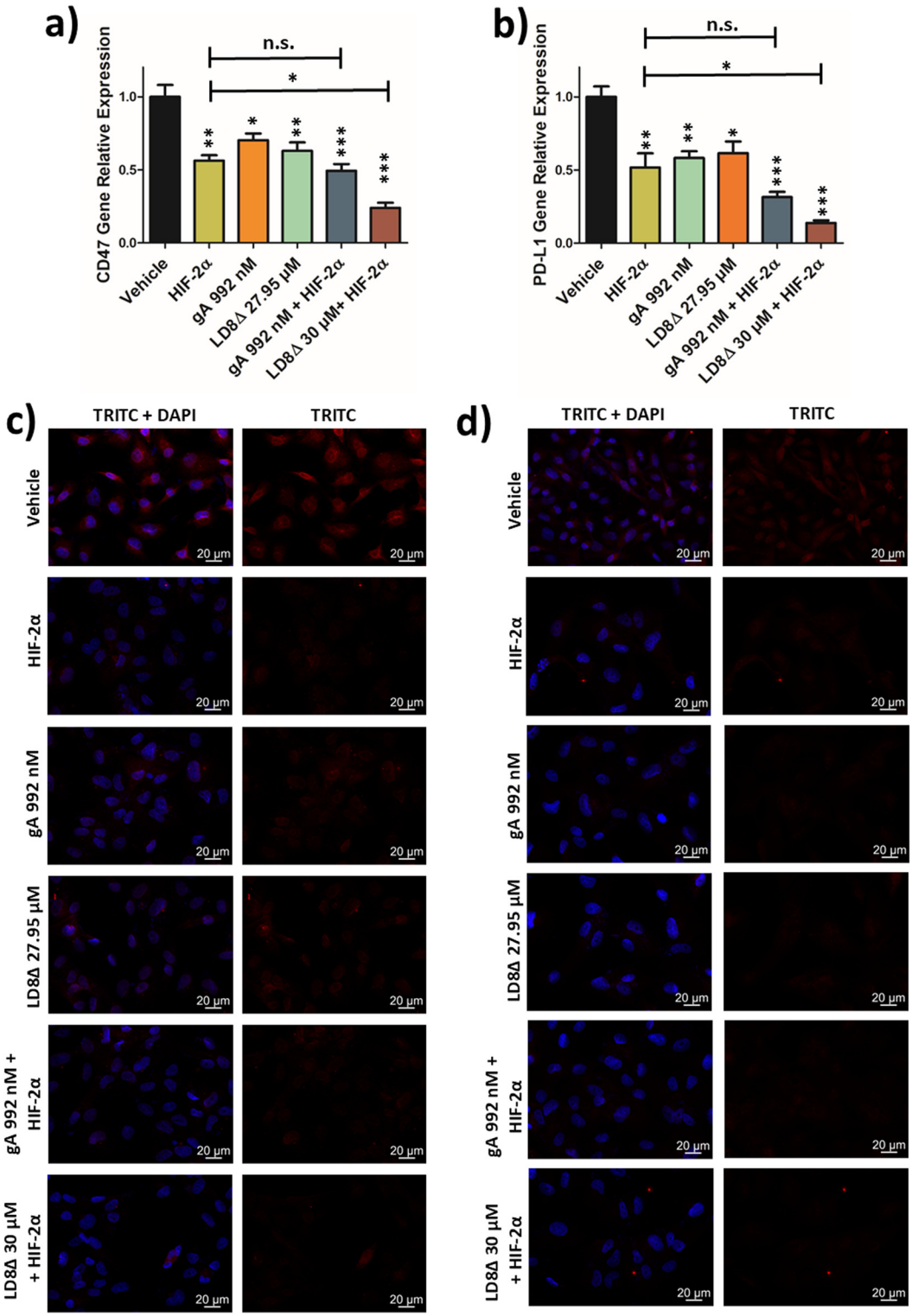

Fig. 7 Relative gene expression of (a) CD47 and (b) PD-L1 in SK-RC-45 cells after treatment with gA, LD8Δ peptide and HIF-2α gene silencing, both in monotherapy and combination therapy at 72 h time point using real-time PCR. Interestingly, only the combination therapy involving LD8Δ peptide and HIF-2α gene silencing exhibited significant reduction in both CD47 and PD-L1 gene expressions compared with monotherapy using HIF-2α gene silencing. *p* values are based on one-way ANOVA with Bonferroni post-test (*, $p < 0.05$; **, $p < 0.01$; ***, $p < 0.001$; n.s., not significant compared with vehicle). Results are presented as mean ± SEM. Immunofluorescence of (c) CD47 protein and (d) PD-L1 protein after treatment with gA, LD8Δ peptide and HIF-2α gene silencing, both in monotherapy and combination therapy at 72 h time point. Untreated SK-RC-45 cells were considered as vehicles. Scale bar = 20 μM. Both monotherapy and combination therapy significantly decreased the protein expression of CD47 and PD-L1 proteins.

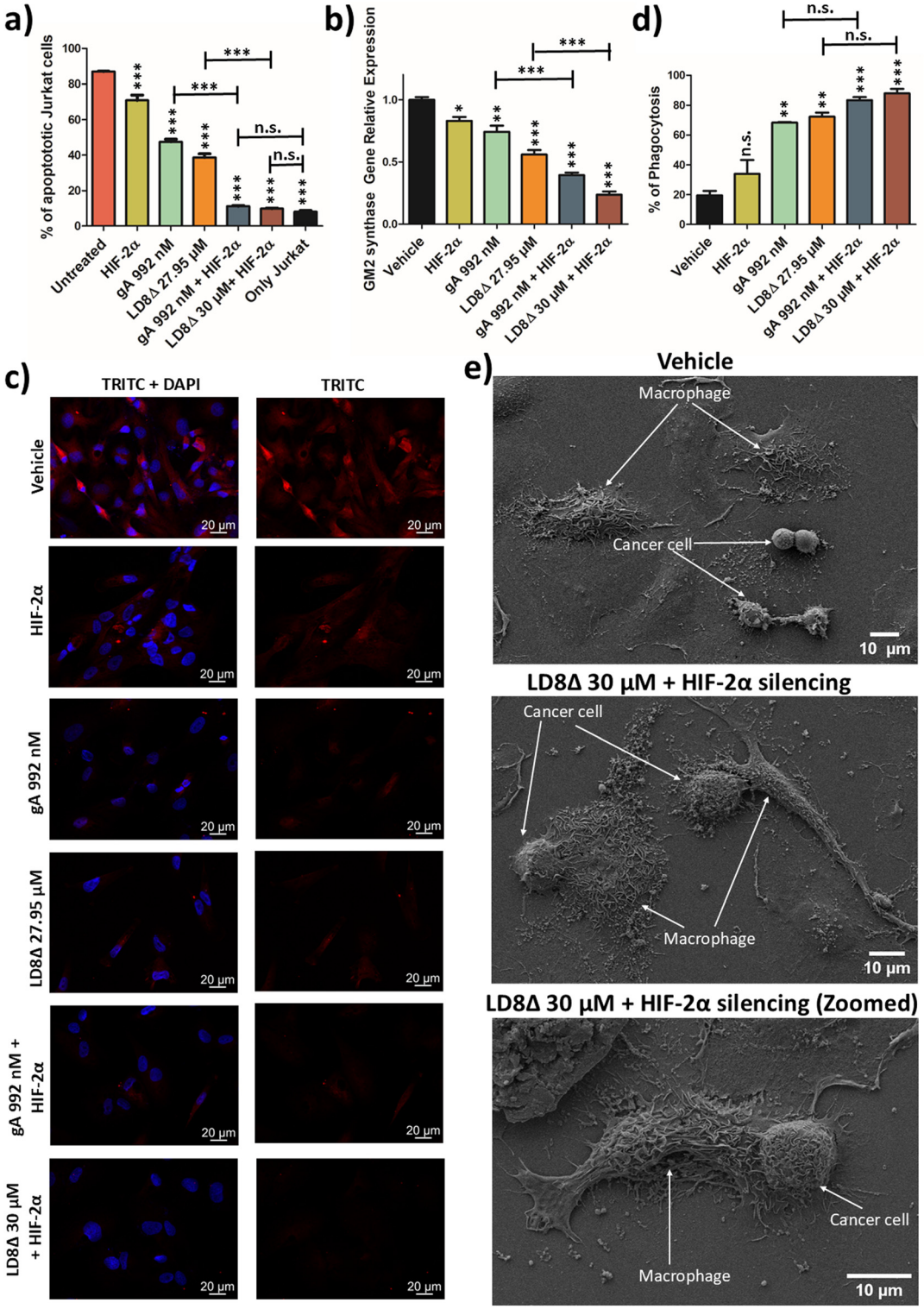

Fig. 8 (a) Percentage of apoptotic Jurkat cells induced by mono- and combination drug-treated SK-RC-45 kidney cancer cells at 72 h. (b) Relative GM2 synthase gene expression in mono- and combination drug-treated SK-RC-45 cells at 72 h time point using real-time PCR. (c) Immunofluorescence of GM2 protein in mono- and combination drug-treated SK-RC-45 cells at 72 h time point compared with untreated SK-RC-45 cells, considered as vehicles. Scale bar = 20 μM. (d) Percentage of macrophages phagocytosing SK-RC-45 kidney cancer cells in a co-culture of SK-RC-45 cells and THP-1 cells for 4 h after treating SK-RC-45 cells with gA, LD8Δ peptide and HIF-2α gene silencing, both in monotherapy and combination therapy for 72 h. Data indicate enhanced phagocytic activity in the presence of both gA and LD8Δ peptide as monotherapy. *p* values are based on one-way ANOVA with Bonferroni post-test (*, $p < 0.05$; **, $p < 0.01$; ***, $p < 0.001$; n.s., not significant compared with untreated in (a) and vehicle in (b) and (d)). Results are presented as mean ± SEM. (e) FE-SEM images revealing phagocytosis of combination drug treated SK-RC-45 cells by THP-1 macrophages.

GM2-synthase is responsible for the production of gangliosides, mainly GM2. Real-time PCR of GM2-synthase will provide sufficient evidence to conclude the production of ganglioside GM2. According to Biswas and group, GM2-synthase is overexpressed in various RCC cell lines, including SK-RC-45.[68] We observed a greater reduction in GM2-synthase gene expression (Fig. 8b and Table 6) and GM2 protein expression (Fig. 8c and Table 4) with combination therapy compared to monotherapy.

2.15.3. Evaluation of *in vitro* phagocytosis of metastatic ccRCC cell line SK-RC-45. This experiment was performed to determine the percentage of macrophages that could phagocytose cancer cells. Park *et al.* reported that CD47 is expressed the highest in ccRCC histological subtypes in comparison to other types of RCC.[65] The high expression of CD47 in cancer cells will restrain macrophages from phagocytosing cancer cells.[62] Given that we observed a decrease in CD47 expression both at the gene and protein levels, after the treatment of both monotherapy and combination therapy (Fig. 7a and c), we were interested to examine that if this treatment can elevate the phagocytosis of metastatic SK-RC-45 cells by macrophages. THP-1 monocyte cells were treated with PMA (phorbol 12-myristate 13-acetate) for their differentiation to macrophages.[69] Additionally, macrophages were polarized to the M2 phenotype by IL-4 administration and were co-incubated with SK-RC-45 cells in a 1 : 4 ratio to mimic tumor conditions.[70–72] Co-incubation of both cells was done for 4 h given that the maximum phagocytosis occurs at 4–6 h of co-incubation.[70,71,73] The percentage of THP-1 cells phagocytosing SK-RC-45 cells was determined by flow cytometry (Fig. 8d). The cancer cells were labelled with CM-Dil, which can be detected by the PI channel, and the macrophages were labelled by CD11b antibody conjugated to FITC.[71] CM-Dil+/CD11b FITC+ cells represent the macrophages that phagocytised cancer cells and CM-Dil−/CD11b FITC+ represent the macrophages that failed to phagocytize any cancer cells. The unstained cells primarily consist of monocytes, which did not differentiate to macrophages and some unstained cancer cells. Treatment of the SK-RC-45 cells with HIF-2α siRNA, gA (992 nM, IC_{50} dose), LD8Δ (27.95 μM, IC_{50} dose), combination therapy of gA 992 nM with HIF-2α silencing and the combination therapy of LD8Δ 30 μM with HIF-2α silencing for 72 h resulted in 34% ± 9.3%, 68.4% ± 0.4%, 72% ± 2.7%, 83.4% ± 2.1% and 88% ± 3% of macrophages exhibiting phagocytosis, respectively (Fig. 8d). Individual images from the flow cytometry analysis for evaluating the phagocytic ability of THP-1 cells for SK-RC-45 cells treated with the individual conditions in this study are depicted in Fig. S9.† Fig. 8d shows that monotherapy promoted considerable phagocytosis, as both gA and LD8Δ could induce apoptotic signature (Fig. 5c) and downregulate CD47 (Fig. 7a) in the SK-RC-45 cell line.[74]

For the *in vitro* visualization of THP-1-mediated phagocytosis, SK-RC-45 cells were treated with a combination of LD8Δ 30 μM and HIF-2α gene silencing and co-incubated with THP-1 cells. The FE-SEM images (Fig. 8e) show that the THP-1 macrophages extended their long thin pseudopods over the combination drug-treated SK-RC-45 cells, demonstrating the process of phagocytosis.

2.16. Assessment of cellular proliferation and micro-metastasis in *in vivo* zebrafish model

All animal procedures were performed in accordance with the Guidelines for Care and Use of Laboratory Animals of IISER Kolkata and approved by the Institutional Animal Ethics Committee (IAEC) under animal use protocol no.: IISERK/IAEC/AP/2022/83. Murine xenograft models are the gold standard in cancer research but are costly and require large cell quantities and time to generate tumours.[31] Thus, to overcome these challenges, we used a zebrafish (*Danio rerio*) xenograft model, which is increasingly popular in cancer research due to its similarities to humans, sharing 71% of protein-coding genes and 82% of disease-related proteins with humans.[31,38] The advantages of zebrafish models include transparent embryos for easy observation, low maintenance costs and the ability to graft human cancer cells into their larvae with an underdeveloped immune system.[31] Additionally, zebrafish embryos can be cultured in small spaces, making them ideal for drug testing. These features make zebrafish a powerful tool for cancer studies and drug evaluation.

A zebrafish xenograft model for human kidney cancer to evaluate the efficacy of LD8Δ and the designed combination therapy was established in this study. SK-RC-45 cells were treated with LD8Δ and a combination of LD8Δ (30 μM) and HIF-2α gene silencing for 72 h. Next, CM-Dil-labelled SK-RC-45 cells were injected into the perivitelline space of zebrafish larvae at 48 h post-fertilization (hpf). A control group of untreated, labelled SK-RC-45 cells was also injected, serving as a vehicle control. Injecting cancer cells into zebrafish larvae can lead to cell proliferation and micro-metastasis, typically toward the tail-fin region.[31,38,75] We monitored the proliferation and micro-metastasis of SK-RC-45 cells at both 0 and 5 days post-injection (dpi) (Fig. 9a and b) by capturing images using epifluorescence microscopy.

The untreated SK-RC-45 cells exhibited significant cell proliferation and migration towards the tail region at 5 dpi (Fig. 9b). However, the larvae injected with LD8Δ (27.95 μM)-treated SK-RC-45 cells showed a marked reduction in cell proliferation compared to the untreated control at 5 dpi. Micro-metastasis was only confined to the yolk sac extension region the in case of the drug-treated SK-RC-45 cells compared to the tail region in the untreated control at 5 dpi (Fig. 9b). Cell proliferation was quantified by measuring the fluorescence intensity of CM-Dil-labelled SK-RC-45 cells (Fig. 9c). The untreated SK-RC-45 cells displayed approximately 2.2 times greater proliferation at 5 dpi compared to 0 dpi, while the LD8Δ cells exhibited 1.1 times greater proliferation at 5 dpi compared to 0 dpi and those treated with combination therapy exhibited 3.4 times less proliferation at 5 dpi compared to 0 dpi (Fig. 9c). To assess micro-metastasis, we captured images of the midsection to tail region of the zebrafish larvae using epifluorescence microscopy with an increased exposure time (700 ms) (Fig. 9b). The larger red spots shown in the insets of the right and

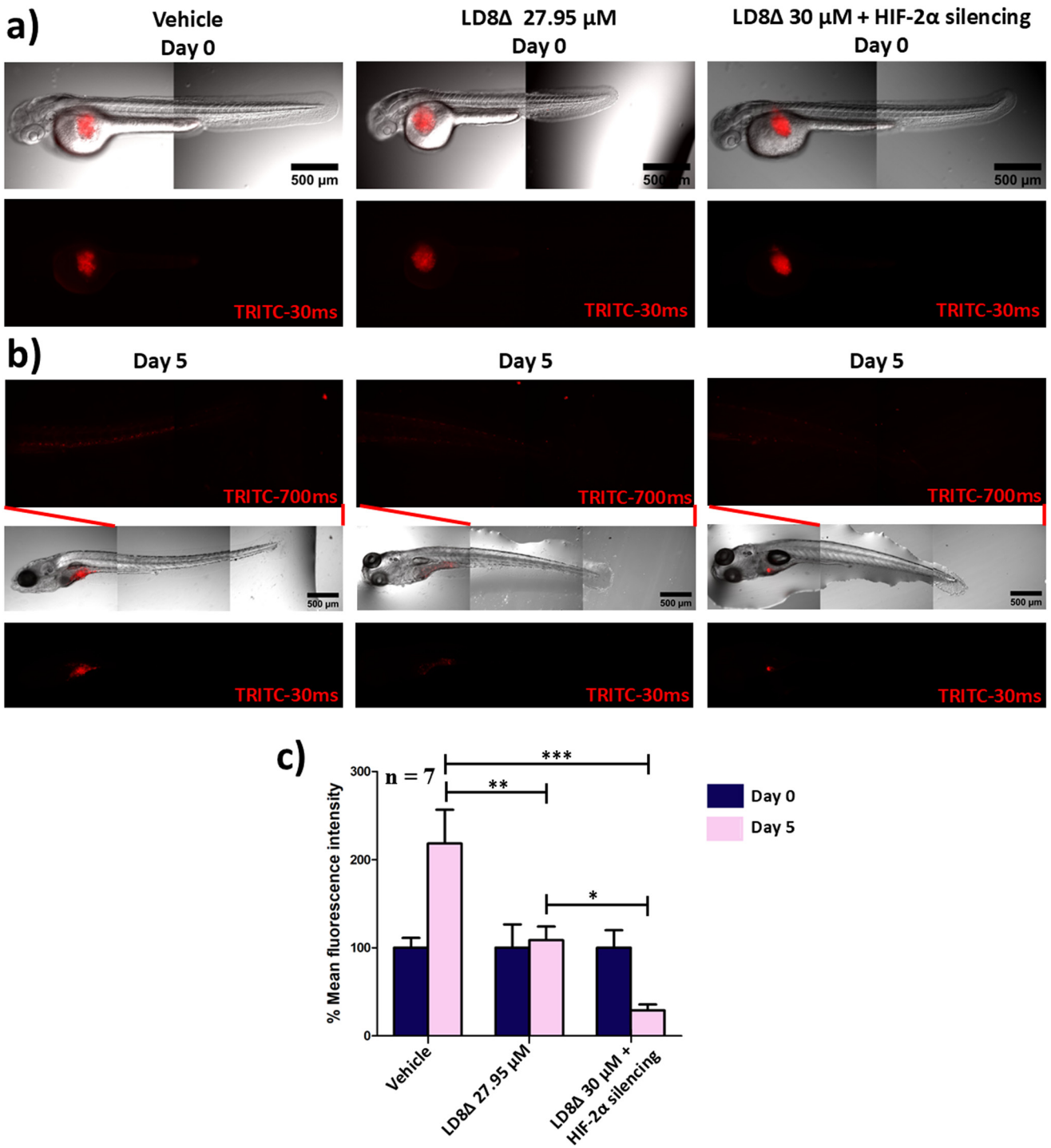

Fig. 9 *In vivo* zebrafish xenograft model for assessing cell proliferation and micro-metastasis in monotherapy (LD8Δ) and combination therapy (LD8Δ + HIF-2α silencing). Images from (a) 0 dpi and (b) 5 dpi, showing zebrafish injected with SK-RC-45 cells: untreated (left), treated with LD8Δ (27.95 μM) for 72 h (centre), and treated with a combination of LD8Δ (30 μM) and HIF-2α gene silencing for 72 h (right). Insets above each condition on 5 dpi are images taken at higher TRITC exposure (700 ms), focusing the middle and tail regions to clearly visualize micro-metastasis. Treatment of SK-RC-45 cells with the designed combination therapy led to a significant reduction in cell proliferation and micrometastasis of SK-RC-45 cells in the *in vivo* zebrafish model compared with the untreated SK-RC-45 cells and those treated with monotherapy. (c) Quantification of SK-RC-45 cell proliferation in the *in vivo* zebrafish xenograft model by measuring the fluorescence intensity of CM-Dil labeled SK-RC-45 cells on the fifth day relative to the day of injection. p values are based on one-way ANOVA with Bonferroni post-test (*, $p < 0.05$; **, $p < 0.01$; ***, $p < 0.001$). Data are expressed as mean ± SEM with $n = 7$ for each data point. The experiment was conducted twice. Fluorescence intensity quantification was performed using the ImageJ software and is presented as percentage of mean fluorescence intensity, with the day 0 measurement serving as the baseline.

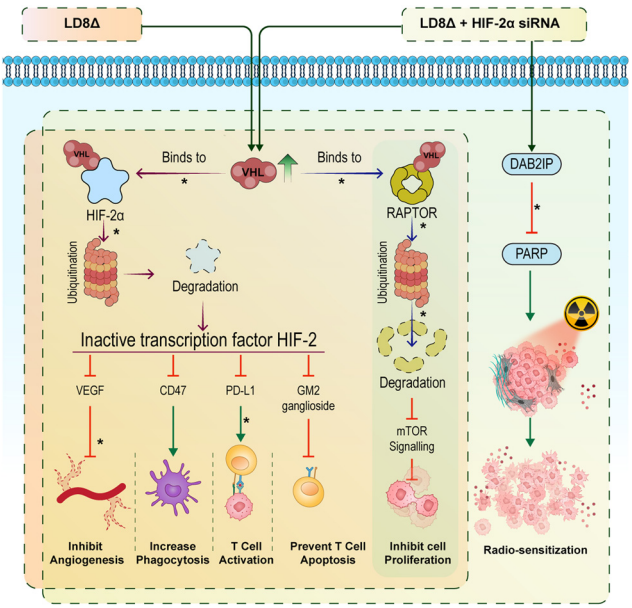

Fig. 10 Cartoon representation based on our studies and literature information, depicting the possible signalling mechanism induced by monotherapy (LD8Δ) and combination therapy (LD8Δ + HIF-2α siRNA). Green pointed arrows indicate upregulation and red blunt arrows indicate downregulation. * indicates information supported by well-known scientific literature. The left panel shows both LD8Δ as monotherapy and LD8Δ and HIF-2α gene silencing as combination therapy upregulated VHL. VHL ubiquitinates both HIF-2α and RAPTOR, leading to the proteosome-mediated degradation of both the proteins, thus inhibiting both HIF-2 (HIF-2α + HIF-β) and mTOR signalling pathways, simultaneously. Inhibition of HIF signalling led to the downregulation of VEGF, CD47, PD-L1 and GM2 gangliosides, resulting in reduced angiogenesis, increased phagocytosis, T cell activation and prevention of T cell apoptosis, respectively. Inhibition of mTOR signalling led to reduced cell proliferation. The right panel indicates that the combination therapy of LD8Δ and HIF-2α gene silencing upregulated the DAB2IP protein, leading to radiosensitization of the metastatic ccRCC cell line SK-RC-45.

middle sections in (Fig. 9b) are residual pigments in the zebrafish larvae and imaging artifacts, not associated with SK-RC-45 cells. Combination therapy of LD8Δ (30 μM) and HIF-2α gene silencing exhibited significant less cellular proliferation of SK-RC-45 compared to monotherapy of LD8Δ (27.95 μM) in an *in vivo* zebrafish xenograft model (Fig. 9c).

A summary of our observations and graphical representation of the probable mechanism of action, obtained from our studies by LD8Δ as monotherapy and by the designed combination therapy of LD8Δ and HIF-2α gene silencing on the metastatic ccRCC SK-RC-45 cell line are presented in Fig. 10.

3. Experimental section

3.1. Materials-

Resin and Fmoc-protected amino acids were procured from Novabiochem and GL Biochem and utilized in the synthesis process without additional purification. Coupling reagents, including HATU, HBTU, and PyBOP, were acquired from Novabiochem, while hydroxybenzotriazole (HOBt) was bought from Sisco Research Laboratories Pvt. Ltd (SRL). Anhydrous dimethylformamide (DMF) and dichloromethane (DCM) employed in the coupling reaction were procured from Acros Organics, and *N*,*N*-diisopropylethylamine (DIPEA) was sourced from TCI Chemicals. The washing solvents DCM and DMF were bought from Merck India. 5(6)-Carboxyfluorescein (FAM) dye was obtained from Invitrogen, and HiPerFect was procured from Qiagen. Dulbecco's modified Eagle's medium (DMEM), fetal bovine serum (FBS), 0.25% trypsin–ethylenediaminetetraacetic acid (EDTA) (1×) and Opti-MEM were obtained from Gibco, Life Technologies. RPMI-1640 and colorless RPMI-1640 were sourced from HiMedia. Gramicidin A, PMA, Fluoroshield with 4′,6-diamidino-2-phenylindole (DAPI), 3-(4,5-dimethylthiazol-2-yl)-2,5-diphenyltetrazolium bromide (MTT) reagent, Triton™ X-100, Rhodamine 123, propidium iodide and cholesterol were procured from Sigma-Aldrich. POPC (cat. no. 850457P) and PE (cat. no. 850757P) for constructing GUVs were sourced from Avanti Polar Lipids. SignalSilence control siRNA (unconjugated) (cat. no. 6568) was obtained from Cell Signaling Technology. Annexin V, Alexa Fluor 488 conjugate (cat. no. A13201), goat anti-rabbit IgG (H + L) secondary antibody, Alexa Fluor 568 (cat. no. A-11036) and CD47 primary antibody (cat. no. MA5-30182) were bought from Thermo Fisher Scientific. VHL (cat. no.: 0377), HIF-2α (cat. no. A7553) and PD-L1 (cat. no. A19135) primary antibodies were procured from ABclonal, USA. BD Pharmingen™ FITC rat anti-CD11b (cat. no. 553310) was procured from BD Biosciences and IL-4 (cat. no. – CYT-211) was obtained from ProSpec-Tany TechnoGene Ltd.

3.2 Peptide synthesis

The Fmoc solid-phase synthesis method was used to prepare the peptides. Coupling of the amino acids was carried out using Fmoc-protected amino acid (5 equivalents), DIC (5 equivalents), and Oxyma (5 equivalents) in dry DMF. We performed double coupling for all the amino acids given that they were hydrophobic. Then, the peptides were lyophilized under vacuum after being purified using reversed-phased HPLC using a C18 column and acetonitrile and water with 0.001% TFA as the purification solvent. Confirmation of the peptide mass was done by MALDI-MS and ESI-MS.

3.3 Cell culture

The ccRCC cell line SK-RC-45, Jurkat, and THP-1 cells were grown in RPMI-1640 medium supplemented with 10% FBS, 1% sodium pyruvate, 1% MEM non-essential amino acids, 1% penicillin–streptomycin and 0.1% amphotericin B. Human fibroblast and HEK-293 cells were cultured in DMEM supplemented with 10% FBS, 1% penicillin–streptomycin, and 0.1% amphotericin B.

3.4. Cell viability assay

Cells were exposed to varying doses of either monotherapy or combination therapy for different intervals, as follows: 24–72 h

for the SK-RC-45 cell line and 72 h for the HEK-293 and human fibroblast cell line, and the MTT assay was performed as mentioned in ref. 30. Data were analysed using GraphPad Prism, and the results are presented as mean ± SEM. The experiments were replicated twice.

3.5. Haemolysis assay

Goat blood was acquired from a local butcher shop and collected in Alsever's solution (2.05% dextrose, 0.8% sodium citrate, and 0.42% sodium chloride) at a ratio of 1 : 5. The haemolysis assay was performed with varying doses of LD8Δ, as mentioned in ref. 76. The absorbance of the supernatants was measured at 540 nm using a UV–vis plate reader to evaluate hemoglobin release. In this experiment, PBS and 1% (v/v) Triton X-100 in PBS were used as the negative (0% release) and positive controls (100% release), respectively. The percentage of hemolysis was calculated as 100 × [(OD540 of sample − OD540 of negative control)/(OD540 of positive control − OD540 of negative control)]. All samples were analysed in triplicate for each experiment, and the averages of two independent experiments ± SEM were plotted using GraphPad Prism.

3.6. Immunogenicity assay

PBMCs were isolated from goat blood acquired from a local butcher shop and cultured, as done previously in ref. 31. The cells were incubated with varying doses of gA and LD8Δ for 72 h. PBS was taken the negative control and concanavalin A (ConA) at 5 μg mL^{-1} was taken as the positive control. The MTT assay was performed and the stimulation index was determined as mentioned in ref. 31.

3.7. Determination of serum stability

The serum stability of LD8Δ was examined in the presence of 10% FBS at 72 h time point following the standard procedures, as reported in ref. 30.

3.8. Plasma membrane mimetic GUV poration assay

Giant unilamellar vesicles (GUVs) mimicking the plasma membrane were prepared using a lipid mixture consisting of phosphatidylcholine (PC), cholesterol, and phosphatidylethanolamine (PE) in a ratio of 65 : 20 : 15 [41] and the gel swelling technique, as mentioned in ref. 31. Then, the GUV solution was incubated with gA at a concentration of 992 nM and LD8Δ at a concentration of 27.95 μM at 37 °C for 1 h and observed under a confocal microscope. A 5 μM concentration of melittin was utilized as the positive control.

3.9. Computational simulation studies

3.9.1. MD simulation of peptide with membrane. A lipid bilayer system consisting of 1-palmitoyl-2-oleoyl-*sn-glycero*-3-phosphocholine (POPC) and 1-palmitoyl-2-oleoyl-*sn-glycero*-3-[phospho-L-serine] (POPS) phospholipids was built using CHARMM-GUI membrane builder[77,78] for the LD8Δ and melittin systems. In both systems, the bilayer consisted of 160 POPC and 40 POPS phospholipids in each leaflet and these compositions were selected because they mimic the cell membrane of cancer cells.[31] The lipid bilayers were solvated with 17707 TIP3P[79] water molecules for the LD8Δ system and 20108 TIP3P water molecules for the melittin system based on their hydration number. The neutralization of the systems was performed by the addition of 150 mM KCl salt. The extended structure of LD8Δ was modelled using Discovery Studio Visualizer and the X-ray crystal structure of melittin was retrieved from the Protein Data Bank using PDB ID: 2MLT. Each peptide molecule (LD8Δ and melittin) was aligned parallel to the bilayer-water interface. The LD8Δ and melittin systems possessed dimensions of 11.62 nm × 11.62 nm × 8.5 nm and 11.67 nm × 11.67 nm × 9.02 nm, respectively. All directions were subjected to periodic boundary conditions. The CHARMM36 forcefield[80] was used for the lipids and peptide molecules in both systems. The energy of the systems was minimized using the steepest descent algorithm.[81] A V-rescale thermostat[82] was used to equilibrate the systems for 3 ns at a temperature of 310 K. Following NVT equilibration, the systems were subjected to NPT equilibration using a Nosé–Hoover thermostat[83,84] and a Parrinello–Rahman barostat[85] for 7 ns at 310 K and 1 bar of pressure. The long-range electrostatic interactions were computed using the particle-mesh Ewald algorithm,[86] while a linear constraint solver (LINCS)[87] algorithm was used to constrain bonds to every atom. The MD simulations were performed for 300 ns using GROMACS 5.1.5.[88]

3.9.2. Calculation of membrane properties. In our case, we estimated the local area per lipid by dividing the membrane into 200 × 200 grids along its *X*–*Y* plane and averaged the last 100 ns of the trajectories for both the LD8Δ peptide and melittin systems using the "FATSLiM" package.[42] Local thickness was calculated similarly to the local APL estimation method, *i.e.*, along a 200 × 200 grid of membrane plane along the *X*–*Y* axis using the FATSLiM package for the LD8Δ and melittin peptide systems. We calculated the mean curvature of the membrane using the Python module "MembraneCurvature" along the *X*–*Y* plane by dividing it into a 6 × 6 grid and plotted an average of the mean curvature values after extrapolating the 6 × 6 grid values into a 24 × 24 grid.

3.9.3. Computational simulation studies of wild-yype and mutant VHL-HIF-2α complex interaction. The X-ray crystal structure of the wild-type VHL-HIF-2α complex was retrieved from the Protein Data Bank using accession ID: 6BVB, which has a resolution of 2.00 Å.[55] A single-point mutation, Arg82Pro,[53] was introduced in VHL, which is specific to the SK-RC-45 renal cell carcinoma (RCC) cell line, to generate a mutant VHL-HIF-2α complex using the mutagenesis module of PyMol version 1.8.x. The simulation cubic box for both the wild-type and mutant VHL-HIF-2α complexes measured 8.6 nm, containing 20 527 and 20 521 TIP3P water molecules, respectively. The wild-type and mutant complexes were neutralized by adding 2 Na^+ ions and 3 Na^+ ions, respectively, and both systems were subjected to energy minimization using the steepest descent algorithm, followed by isochoric–isothermal (NVT) and isothermal–isobaric (NPT) equilibration, each for

100 ps, and a final unrestrained production MD run for 100 ns, as previously described.[89] The total interaction energy (sum of the van der Waals energy and electrostatic energy) between the VHL and HIF-2α proteins in the wild-type and mutant complex was calculated using the g_mmpbsa tool.[90]

3.10. Mitochondrial depolarization assay

Cells were plated in 6-well plates at a density of 0.25×10^6 cells per well. On the following day, the cells were exposed to various concentrations of monotherapies and combination therapies and incubated for 72 h. The mitochondrial depolarization assay was performed as mentioned in ref. 30 and analysed using flow cytometry (BD LSRFortessa™). The flow cytometry data was analysed using the BD FACSDiva™ software and further processed using the GraphPad Prism software. The data is represented as mean ± SEM of two independent experiments.

3.11. Cell cycle analysis with PI

0.25×10^6 cells were seeded in each well of a 6-well plate, followed by treatment with various doses of monotherapies and combination therapies for a duration of 72 h. The cells were trypsinized and the resulting cell suspension was collected *via* centrifugation. The harvested cells were fixed with 100% ethanol and incubated for 2 h at 4 °C. After the removal of ethanol, the cells were washed with chilled PBS and stained with PI at a final concentration of 40 μg mL^{-1}, followed by a 10 min incubation at 4 °C. Subsequently, the cells were analysed using a BD LSRFortessa™ flow cytometer. Calibration was done by BD™ DNA QC particles consisting of chicken erythrocyte nuclei (CEN) and calf thymocyte nuclei (CTN). Data analysis was done using the BD FACSDiva™ software, and the results were plotted using GraphPad Prism. The data is represented as the mean ± SEM from two separate experiments.

3.12. Apoptosis/necrosis assay

Apoptosis and necrosis were assessed using Annexin V, Alexa Fluor 488 conjugate combined with propidium iodide (PI) staining, as mentioned in ref. 30. 0.25×10^6 cells were cultured in 6-well plates and treated with monotherapies and combination therapies at various concentrations for 72 h. The cells were analysed using a BD LSRFortessa™ instrument. Data analysis was done using the BD FACSDiva™ software. The experiment was conducted in duplicate, and the results were plotted using GraphPad Prism software. The data is represented as the mean ± SEM from two separate experiments.

3.13. Clonogenic assay

Untreated SK-RC-45 cells, SK-RC-45 cells treated with the combination of 30 μM LD8Δ and HIF-2α gene silencing for 72 h and non-cancerous human fibroblast cells were cultured in two sets. The cells of one set were irradiated with 2 Gy radiation by VitalBeam™ (Varian Medical System) using 6 MV X-rays. No radiation was applied to the other set. Then, the cells were replated in triplicate for each condition in 100 mm plates at a density of 1000 cells per 100 mm plate to form colonies. After 14 days, the cells were fixed with methanol : acetic acid (3 : 1) and stained with 0.5% w/v crystal violet (aqueous solution). Colonies of only 50 or more cells were scored. Colonies were counted using a stereo microscope (Radical RSMr-3B) and photographed with a Nikon D7500 camera. To determine the SF (surviving fraction), the PE (plating efficiency) was first determined. PE and SF were calculated using the formulas PE = number of colonies formed/number of cells seeded and SF = number of colonies formed after treatment/(number of cells seeded × PE).[47] All samples were analysed in triplicate for each experiment, and the average of two independent experiments ± SEM was plotted using GraphPad Prism.

3.14. Realtime PCR analysis

The relative gene expression levels of VHL, HIF-2α, HIF-1α, VEGF, mTOR, DAB2IP, CD47, PD-L1 and GM2 synthase were assessed *via* real-time PCR after treating SK-RC-45 cells with varying doses of monotherapies and combination therapies for 72 h. RNA extraction was done using the RNeasy mini kit (Qiagen). Subsequently, the RNA was reverse-transcribed into cDNA using the Verso cDNA synthesis kit (Thermo Fisher Scientific). Real-time PCR analysis of the target mRNA expressions was conducted using the SYBR green detection method in a CFX96™ real-time system (Bio-Rad). The primer sequences utilized for PCR amplification are provided in Table S1.† Primer synthesis was conducted by Eurofins Genomics India Pvt. Ltd. HIF-2α silencing siRNA was also synthesized by Eurofins Genomics India Pvt. Ltd. The sequence of HIF-2α silencing siRNA is 5′-UCACAGAACUGAUUGGUUAdTdT-3′ (sense) and 5′-UAACCAAUCAGUUCUGUGAdTdT-3′ (antisense).[91] The resulting data were analyzed and visualized using the GraphPad Prism software and presented as the mean ± SEM from three independent replicates.

3.15. Immunofluorescence studies

SK-RC-45 cells (25 000 cells per well) were seeded on coverslips in 24-well plates. The cells were prepared for immunostaining following the procedure mentioned in ref. 92 with the respective primary antibodies (VHL, HIF-2α, CD47, PD-L1 and GM2 proteins) at a dilution of 1 : 100 overnight at 4 °C. The cells were treated with Alexa Fluor 568 conjugated secondary antibody and mounted with Fluoroshield-containing DAPI (Sigma-Aldrich) onto a glass slide and observed under an Apotome microscope.

3.16. Determination of apoptotic Jurkat cell population in co-culture

SK-RC-45 cells were treated with varying concentrations of monotherapies and combination therapies for a duration of 72 h. After, the dead floating cells were discarded and only the attached cells were plated in 6 well plates. After 1 h, Jurkat cells were co-cultured in the 6 well plates together with the SK-RC-45 cells at a ratio 1 : 3 for 72 h in complete RPMI media

for 72 h. Only the Jurkat cells were removed by gentle washing and analyzed to determine the apoptotic population by Annexin V conjugated with Alexa Fluor 488/PI staining, as discussed in ref. 30.

3.17. Determination of phagocytosis percentage

THP-1 monocyte cells were induced to differentiate to macrophages by incubating with phorbol 12-myristate 13-acetate (PMA), 100 ng mL^{-1} for 48 h.[69] After 48 h, the PMA-containing media was discarded and cells were allowed to rest for 24 h. Following which, the cells were incubated with interleukin-4 at a dose of 20 ng mL^{-1} for 24 h.[72] Then, the medium containing IL-4 was discarded and fresh medium was added. In separate cell culture plates, SK-RC-45 cells were treated with varying concentrations of monotherapies and combination therapies for a duration of 72 h. Then, the SK-RC-45 cells were labelled with 2 μM CM-Dil stain following the product's instruction manual. The stained SK-RC-45 cells were co-cultured with THP-1 cells in the 6-well plates pre-treated with PMA and IL-4 at 4 : 1 ratio for 4 h. The cells in the co-culture were scraped using a cell-scraper and collected in ice-cold PBS supplemented with 5% FBS (v/v). Then, the cells were centrifuged at 1200 rpm for 4 min at 4 °C. The supernatant was discarded and fresh ice-cold PBS supplemented with 5% FBS (v/v) was added. To this, 0.25 μL of CD11b-FITC conjugated antibody was incubated for 30 min in ice to stain the macrophage cells. The cells were collected by centrifugation, followed by washing to avoid any excess CD11b-FITC conjugate and analyzed using a BD LSRFortessa™ instrument. Data analysis was performed using the BD FACSDiva™ software (from BD Biosciences). The experiment was conducted in duplicate, and the results were plotted using the GraphPad Prism software. The data are expressed as the mean ± SEM of two separate experiments.

3.18. Determination of phagocytosis by FE-SEM

A co-culture of THP-1 and SK-RC-45 cells was prepared as mentioned in the previous section (3.17). Untreated SK-RC-45 cells and SK-RC-45 cells treated with combination of LD8Δ 30 μM and HIF-2α silencing for 72 h were used. The FE-SEM experiment was performed as mentioned in ref. 76. The experiment was repeated twice.

3.19. Zebrafish xenograft studies

All animal procedures were performed in accordance with the Guidelines for Care and Use of Laboratory Animals of IISER Kolkata and approved by the Institutional Animal Ethics Committee (IAEC) under animal use protocol no.: IISERK/IAEC/AP/2022/83. For monotherapy, SK-RC-45 cells were treated with LD8Δ (27.95 μM) for 72 h, and for combination therapy, SK-RC-45 cells were treated with LD8Δ (30 μM) together with HIF-2α gene silencing for 72 h. The, cells were then stained and microinjected into the perivitelline space of a 48 hpf zebrafish embryo, as done previously.[31] Post-image processing including quantification of the fluorescence intensity and image stitching was done using the ImageJ software. The experiment was repeated twice and the data was plotted using the GraphPad Prism software considering the fluorescent intensity of 0 dpi as the baseline.

4. Conclusions

Our study demonstrated that the LD8Δ peptide is biocompatible and non-hemolytic and has significant potential to be used as oral cancer medicine. Our designed combination therapy having the LD8Δ peptide and HIF-2α gene silencing siRNA exhibited strong synergistic drug interactions, inducing a high level of apoptosis in ccRCC cells, mitochondrial depolarization and cell cycle arrest. Additionally, our designed combination therapy downregulated the major oncogenes VEGF, mTOR and multi-oncogenic switch HIF-2α, confirming the prevention of cancer metastasis both in *in vitro* and *in vivo* zebrafish models. Interestingly, it also sensitized radioresistant SK-RC-45 cells to radiotherapy. Our studies showed that the designed combination therapy potentiated immunotherapy against SK-RC-45 cells by dual activation of macrophages and T cells. The significant findings of our present study demonstrated that peptide-based proton transporters can be considered a new class of anti-cancer drugs having unique potential for radiosensitization and potentiating immunotherapy. Our designed cost-effective protease-stable multifunctional anti-cancer therapeutics may have great translational potential to treat patients having aggressive radioresistant kidney cancer.

Author contributions

R. S. R. and A. M. M. conceptualized the manuscript and designed the experiments. A. M. M. performed all wet lab experiments. A. C. helped A. M. M. in these wet lab experiments. A. T. synthesized the peptides. M. H. managed zebrafish care and assisted with their breeding. Computational studies were designed by R. S. R., A. S., A. B. G., P. U. and A. M. M. and performed by A. S., P. U. and A. B. G. The entire manuscript except the computational part was written by A. M. M. and R. S. R. The computational part was written by A. S., P. U. and A. B. G.

Data availability

The experimental and computational data supporting this article and the characterization data like mass spectra are provided in the ESI.†

Conflicts of interest

The authors declare the following competing financial interests: Sinha Roy R., Srivastava A., Mallick A. M., Chatterjee A., Gurung A. B., Uttarasili P., Tripathi A., Hembram M. Indian Institute of Science Education and Research Kolkata. Pharmaceutical Composition for Treatment of Kidney Cancer.

Indian patent application no. 202533004009 (patent of addition to granted Indian patent number – 444719). 2025 Jan 17.

Acknowledgements

This research was supported partially by DBT Nanobiotechnology (BT/PR22086/NNT/28/1222/2017) and partially by DST SERB POWER (grant no.: SPF/2021/000024). RSR thanks DBT Nanobiotechnology (BT/PR22086/NNT/28/1222/2017) for the computational part of the project done at IISER Kolkata. AS acknowledges the high-performance computing facility "Beagle" that was set up from grants by the partnership between the Department of Biotechnology of India and the Indian Institute of Science (IISc-DBT partnership programme). AS thanks the DST for the National Supercomputing Mission grants (DST/NSM/R/&D-HPC-Applications/2021/03.10, DST/NSM/R/&D-HPC-Applications/Extension Grant/2023/27). AS also thanks the DST for the FIST program sponsored by the Department of Science and Technology. AS would also like to thank the Teams Science Grant from the DBT-Wellcome Trust India Alliance (grant number: IA/TSG/21/1/600245). AS thanks the DBT National Network Project (NNP) grant (BT/PR40323/BTIS/137/78/2023) and the Matrics grants (MTR/2023/001040) from the Science and Engineering Board (SERB), India. AMM, PU and MH thank CSIR for the fellowship. AMM also thanks DBT Nanobiotechnology (BT/PR27059/NNT/28/1543/2017) for the financial support. AC is grateful to UGC for the fellowship. ABG is thankful to IISER Kolkata Post-doctoral Fellowship, and AT thanks IISER Kolkata for her fellowship. RSR is grateful to DST SERB for the SERB POWER fellowship (grant no.: SPF/2021/000024). The authors express their sincere thanks to Prof. Kaushik Biswas (Bose Inst, India) for providing the SK-RC-45 cell line and Dr Gregory Raskin (MSKCC, USA) for his kind approval, Dr Dipyaman Ganguly (IICB, India) for providing the Jurkat cell line and Dr Rohan Dhiman (NIT Rourkella, India) for providing the THP-1 cell line as a kind gift. Special thanks to Prof. Srikrishna Mandal (NRSMC, India), Mr Angshuman Roy (Dept of Radio Therapy, NRSMC, India) and Mr Sandeep Ghosh (Dept of Radio Therapy, NRSMC, India) for their assistance in applying radiation to cells. The authors are grateful to Dr Rupnarayan Bhattacharya (RGKMCH, India) for connecting us to NRSMC, India for applying radiation to cells and Prof. Deepak Kumar Sinha (IACS, India) for getting us the THP-1 cell line. The authors also thank Prof. Krishanu Ray (NBRC and TIFR, India) and Dr Sumanta Basu (BD Biosciences) for valuable discussions. The authors thank Prof. Jonaki Sen (IIT Kanpur) for providing glass capillaries for making needles for nano-injection. We sincerely thank Mr Amarendra Nath Biswas (MALDI-MS facility, Bose Institute, India), Mr Paramananda Patel (IISER-K ESI-MS central facility) and Mrs Tania Roy (IISER Kolkata, India) for mass spectrometry data, Mr Kashinath Sahu (IISER-K SEM facility) for SEM data, Mr Ritabrata Ghosh (IISER-K imaging facility) for ApoTome and confocal microscopy and Mr Tamal Ghosh (IISER-K flow cytometry facility) for flow cytometry data. The authors thank Dr Gopikrishna J for his assistance in creating Fig. 1 and 10 for this manuscript. TOC is created with the help of BioRender.com. Authors dedicate this manuscript to Professor Raghavan Varadarajan (Molecular Biophysics Unit, Indian Institute of Science, Bangalore) on his 65th birthday.

References

1 L. Cirillo, S. Innocenti and F. Becherucci, Global epidemiology of kidney cancer, *Nephrol., Dial., Transplant.*, 2024, **39**(6), 920–928.
2 L. Dahman, V. Gauthier, A. Camier, J. J. Bigna, F. Glowacki, P. Amouyel, L. Dauchet and A. Hamroun, Air pollution and kidney cancer risk: a systematic review and meta-analysis, *J. Nephrol.*, 2024, 1–12.
3 B. Tanriover, Renal cell cancer, environmental arsenic exposure and carcinogenic mutations, *Int. J. Hematol. Oncol.*, 2012, **33**(1), 062–066.
4 J. J. Hsieh, M. P. Purdue, S. Signoretti, C. Swanton, L. Albiges, M. Schmidinger, D. Y. Heng, J. Larkin and V. Ficarra, Renal cell carcinoma, *Nat. Rev. Dis. Primers*, 2017, **3**(1), 1–19.
5 N. Shenoy and L. Pagliaro, Sequential pathogenesis of metastatic VHL mutant clear cell renal cell carcinoma: putting it together with a translational perspective, *Ann. Oncol.*, 2016, **27**(9), 1685–1695.
6 Y. Wang, Y. Zhang, P. Wang, X. Fu and W. Lin, Circular RNAs in renal cell carcinoma: implications for tumorigenesis, diagnosis, and therapy, *Mol. Cancer*, 2020, **19**(1), 1–10.
7 H. Koul, J.-S. Huh, K. O. Rove, L. Crompton, S. Koul, R. B. Meacham and F. J. Kim, Molecular aspects of renal cell carcinoma: a review, *Am. J. Cancer Res.*, 2011, **1**(2), 240.
8 Y. Jian, K. Yang, X. Sun, J. Zhao, K. Huang, A. Aldanakh, Z. Xu, H. Wu, Q. Xu and L. Zhang, Current advance of immune evasion mechanisms and emerging immunotherapies in renal cell carcinoma, *Front. Immunol.*, 2021, **12**, 639636.
9 T. K. Choueiri and R. J. Motzer, Systemic therapy for metastatic renal-cell carcinoma, *N. Engl. J. Med.*, 2017, **376**(4), 354–366.
10 R. J. Motzer, T. E. Hutson, P. Tomczak, M. D. Michaelson, R. M. Bukowski, O. Rixe, S. Oudard, S. Negrier, C. Szczylik and S. T. Kim, Sunitinib versus interferon alfa in metastatic renal-cell carcinoma, *N. Engl. J. Med.*, 2007, **356**(2), 115–124.
11 R. J. Motzer, T. E. Hutson, D. Cella, J. Reeves, R. Hawkins, J. Guo, P. Nathan, M. Staehler, P. de Souza and J. R. Merchan, Pazopanib versus sunitinib in metastatic renal-cell carcinoma, *N. Engl. J. Med.*, 2013, **369**(8), 722–731.
12 R. J. Motzer, B. Escudier, S. Oudard, T. E. Hutson, C. Porta, S. Bracarda, V. Grünwald, J. A. Thompson, R. A. Figlin and N. Hollaender, Phase 3 trial of everolimus for metastatic renal cell carcinoma: final results and analysis of prognostic factors, *Cancer*, 2010, **116**(18), 4256–4265.

13 I. J. Frew and H. Moch, A clearer view of the molecular complexity of clear cell renal cell carcinoma, *Annu. Rev. Pathol.: Mech. Dis.*, 2015, **10**, 263–289.
14 R. J. Motzer and P. Russo, Systemic therapy for renal cell carcinoma, *J. Urol.*, 2000, **163**(2), 408–417.
15 G. Banumathy and P. Cairns, Signaling pathways in renal cell carcinoma, *Cancer Biol. Ther.*, 2010, **10**(7), 658–664.
16 V. H. Haase, Renal cancer: oxygen meets metabolism, *Exp. Cell Res.*, 2012, **318**(9), 1057–1067.
17 A. McIntyre, A. Hulikova, I. Ledaki, C. Snell, D. Singleton, G. Steers, P. Seden, D. Jones, E. Bridges and S. Wigfield, Disrupting hypoxia-induced bicarbonate transport acidifies tumor cells and suppresses tumor growth, *Cancer Res.*, 2016, **76**(13), 3744–3755.
18 O. Lombardi and D. R. Mole, HIF pathways in clear cell renal cancer, in *Biomarkers and Bioanalysis Overview*, IntechOpen, 2021.
19 E. Jonasch, F. Donskov, O. Iliopoulos, W. K. Rathmell, V. K. Narayan, B. L. Maughan, S. Oudard, T. Else, J. K. Maranchie and S. J. Welsh, Belzutifan for renal cell carcinoma in von Hippel–Lindau disease, *N. Engl. J. Med.*, 2021, **385**(22), 2036–2046.
20 L. Davis, M. Recktenwald, E. Hutt, S. Fuller, M. Briggs, A. Goel and N. Daringer, Targeting HIF-2α in the tumor microenvironment: redefining the role of HIF-2α for solid cancer therapy, *Cancers*, 2022, **14**(5), 1259.
21 T. Bose, A. Cieślar-Pobuda and E. Wiechec, Role of ion channels in regulating Ca2+ homeostasis during the interplay between immune and cancer cells, *Cell Death Dis.*, 2015, **6**(2), e1648–e1648.
22 J. M. David, T. A. Owens, S. P. Barwe and A. K. Rajasekaran, Gramicidin A induces metabolic dysfunction and energy depletion leading to cell death in renal cell carcinoma cells, *Mol. Cancer Ther.*, 2013, **12**(11), 2296–2307.
23 A. M. Mallick, K. Chakraborty, A. Biswas, S. Jan, C. Dutta, S. Dey, S. Sahoo, K. Mandal and R. Sinha Roy, Emerging peptide-based technologies in cancer therapy, in *Unravelling Cancer Signaling Pathways: A Multidisciplinary Approach*, 2019, pp. 13–49.
24 Y. Takada, H. Itoh, A. Paudel, S. Panthee, H. Hamamoto, K. Sekimizu and M. Inoue, Discovery of gramicidin A analogues with altered activities by multidimensional screening of a one-bead-one-compound library, *Nat. Commun.*, 2020, **11**(1), 4935.
25 R.-Q. Wang, J. Geng, W.-J. Sheng, X.-J. Liu, M. Jiang and Y.-S. Zhen, The ionophore antibiotic gramicidin A inhibits pancreatic cancer stem cells associated with CD47 down-regulation, *Cancer Cell Int.*, 2019, **19**, 1–13.
26 K. Chakraborty, A. Tripathi, S. Mishra, A. M. Mallick and R. S. Roy, Emerging concepts in designing next-generation multifunctional nanomedicine for cancer treatment, *Biosci. Rep.*, 2022, **42**(7), BSR20212051.
27 N. Santos, J. B. Wenger, P. Havre, Y. Liu, R. Dagan, I. Imanirad, A. M. Ivey, R. A. Zlotecki, C. B. Algood and S. M. Gilbert, Combination therapy for renal cell cancer: what are possible options?, *Oncology*, 2011, **81**(3–4), 220–229.
28 C. Buonerba, G. Di Lorenzo and G. Sonpavde, Combination therapy for metastatic renal cell carcinoma, *Ann. Transl. Med.*, 2016, **4**(5), 100.
29 T. Chen, Y. Wang, Y. Yang, K. Yu, X. Cao, F. Su, H. Xu, Y. Peng, Y. Hu and F. Qian, Gramicidin inhibits human gastric cancer cell proliferation, cell cycle and induced apoptosis, *Biol. Res.*, 2019, **52**, 57.
30 K. Chakraborty, C. Dutta, S. Mukherjee, A. Biswas, P. Gayen, G. George, S. Raghothama, S. Ghosh, S. Dey and D. Bhattacharyya, Engineering ionophore gramicidin–inspired self–assembled peptides for drug delivery and cancer nanotherapeutics, *Adv. Ther.*, 2018, **1**(7), 1800018.
31 A. M. Mallick, A. Biswas, S. Mishra, S. Jadhav, K. Chakraborty, A. Tripathi, A. Mukherjee and R. S. Roy, Engineered vitamin E-tethered non-immunogenic facial lipopeptide for developing improved siRNA based combination therapy against metastatic breast cancer, *Chem. Sci.*, 2023, **14**(29), 7842–7866.
32 C. Shen and W. G. Kaelin Jr, in *The VHL/HIF axis in clear cell renal carcinoma*, Elsevier, 2013, pp. 18–25, *seminars in cancer biology*.
33 A. M. Mallick, A. Tripathi, S. Mishra, A. Mukherjee, C. Dutta, A. Chatterjee and R. Sinha Roy, Emerging approaches for enabling RNAi therapeutics, *Chem. – Asian J.*, 2022, **17**(16), e202200451.
34 A. Finkelstein and O. S. Andersen, The gramicidin A channel: a review of its permeability characteristics with special reference to the single-file aspect of transport, *J. Membr. Biol.*, 1981, **59**(3), 155–171.
35 E. Diamanti, E. Gutiérrez-Pineda, N. Politakos, P. Andreozzi, M. J. Rodriguez-Presa, W. Knoll, O. Azzaroni, C. A. Gervasi and S. E. Moya, Gramicidin ion channels in a lipid bilayer supported on polyelectrolyte multilayer films: an electrochemical impedance study, *Soft Matter*, 2017, **13**(47), 8922–8929.
36 T.-C. Chou and N. Martin, The mass-action law-based new computer software, CompuSyn, for automated simulation of synergism and antagonism in drug combination studies, *Cancer Res.*, 2007, **67**(9_Supplement), 637–637.
37 T.-C. Chou, Drug combination studies and their synergy quantification using the Chou-Talalay method, *Cancer Res.*, 2010, **70**(2), 440–446.
38 K. Chakraborty, A. Biswas, S. Mishra, A. M. Mallick, A. Tripathi, S. Jan and R. Sinha Roy, Harnessing Peptide-Functionalized Multivalent Gold Nanorods for Promoting Enhanced Gene Silencing and Managing Breast Cancer Metastasis, *ACS Appl. Bio Mater.*, 2023, **6**(2), 458–472.
39 I. V. Bijnsdorp, E. Giovannetti and G. J. Peters, Analysis of drug interactions, in *Cancer Cell Culture: Methods and Protocols*, 2011, pp. 421–434.
40 J. M. David and A. K. Rajasekaran, Gramicidin A: a new mission for an old antibiotic, *J. Kidney Cancer VHL*, 2015, **2**(1), 15.
41 A. Erazo-Oliveras, K. Najjar, D. Truong, T.-Y. Wang, D. J. Brock, A. R. Prater and J.-P. Pellois, The late endosome and its lipid BMP act as gateways for efficient cytosolic

access of the delivery agent dfTAT and its macromolecular cargos, *Cell Chem. Biol.*, 2016, **23**(5), 598–607.
42 S. Buchoux, FATSLiM: a fast and robust software to analyze MD simulations of membranes, *Bioinformatics*, 2017, **33**(1), 133–134.
43 Y.-W. Xue, H. Itoh, S. Dan and M. Inoue, Gramicidin A accumulates in mitochondria, reduces ATP levels, induces mitophagy, and inhibits cancer cell growth, *Chem. Sci.*, 2022, **13**(25), 7482–7491.
44 M. S. Choi, C. Y. Lee, J. H. Kim, Y. M. Lee, S. Lee, H. J. Kim and K. Heo, Gramicidin, a Bactericidal Antibiotic, Is an Antiproliferative Agent for Ovarian Cancer Cells, *Medicina*, 2023, **59**(12), 2059.
45 D. Wlodkowic, W. Telford, J. Skommer and Z. Darzynkiewicz, Apoptosis and beyond: cytometry in studies of programmed cell death, *Methods Cell Biol.*, 2011, **103**, 55–98.
46 S. L. Fink and B. T. Cookson, Apoptosis, pyroptosis, and necrosis: mechanistic description of dead and dying eukaryotic cells, *Infect. Immun.*, 2005, **73**(4), 1907–1916.
47 N. A. Franken, H. M. Rodermond, J. Stap, J. Haveman and C. Van Bree, Clonogenic assay of cells in vitro, *Nat. Protoc.*, 2006, **1**(5), 2315–2319.
48 S. Siva, G. Kothari, A. Muacevic, A. V. Louie, B. J. Slotman, B. S. Teh and S. S. Lo, Radiotherapy for renal cell carcinoma: renaissance of an overlooked approach, *Nat. Rev. Urol.*, 2017, **14**(9), 549–563.
49 J. S. Hall, R. Iype, J. Senra, J. Taylor, L. Armenoult, K. Oguejiofor, Y. Li, I. Stratford, P. L. Stern and M. J. O'Connor, Investigation of radiosensitivity gene signatures in cancer cell lines, *PLoS One*, 2014, **9**(1), e86329.
50 S. I. Kim, J. W. Kang, J. K. Noh, H. R. Jung, Y. C. Lee, J. W. Lee, M. Kong and Y.-G. Eun, Gene signature for prediction of radiosensitivity in human papillomavirus-negative head and neck squamous cell carcinoma, *Radiat. Oncol. J.*, 2020, **38**(2), 99.
51 F. Evans, J. A. Hernández, F. Cabo and S. Chifflet, A Note of Caution: Gramicidin Affects Signaling Pathways Independently of Its Effects on Plasma Membrane Conductance, *BioMed Res. Int.*, 2021, **2021**, 2641068.
52 J. M. David, T. A. Owens, L. J. Inge, R. M. Bremner and A. K. Rajasekaran, Gramicidin A blocks tumor growth and angiogenesis through inhibition of hypoxia-inducible factor in renal cell carcinoma, *Mol. Cancer Ther.*, 2014, **13**(4), 788–799.
53 R. Gemmill, M. Zhou, L. Costa, C. Korch, R. Bukowski and H. Drabkin, Synergistic growth inhibition by Iressa and Rapamycin is modulated by VHL mutations in renal cell carcinoma, *Br. J. Cancer*, 2005, **92**(12), 2266–2277.
54 M. R. Alves, F. C. Carneiro, A. M. Lavorato-Rocha, W. H. Da Costa, I. W. Da Cunha, S. de Cássio Zequi, G. C. Guimaraes, F. A. Soares, D. M. Carraro and R. M. Rocha, Mutational status of VHL gene and its clinical importance in renal clear cell carcinoma, *Virchows Archiv*, 2014, **465**, 321–330.
55 D. Tarade, C. M. Robinson, J. E. Lee and M. Ohh, HIF-2α-pVHL complex reveals broad genotype-phenotype correlations in HIF-2α-driven disease, *Nat. Commun.*, 2018, **9**(1), 3359.
56 I. J. Frew, Z. Smole, C. R. Thoma and W. Krek, Genetic deletion of the long isoform of the von Hippel–Lindau tumour suppressor gene product alters microtubule dynamics, *Eur. J. Cancer*, 2013, **49**(10), 2433–2440.
57 Y. Ye, S. Vasavada, I. Kuzmin, T. Stackhouse, B. Zbar and B. R. Williams, Subcellular localization of the von Hippel–Lindau disease gene product is cell cycle–dependent, *Int. J. Cancer*, 1998, **78**(1), 62–69.
58 Z. Guillaume, M. Auvray, Y. Vano, S. Oudard, D. Helley and L. Mauge, Renal carcinoma and angiogenesis: therapeutic target and biomarkers of response in current therapies, *Cancers*, 2022, **14**(24), 6167.
59 A. P. Ghosh and S. Sudarshan, Genetics of renal cancer: Focus on MTOR, *Aging*, 2016, **8**(3), 421.
60 A. Ganner, C. Gehrke, M. Klein, L. Thegtmeier, T. Matulenski, L. Wingendorf, L. Wang, F. Pilz, L. Greidl and L. Meid, VHL suppresses RAPTOR and inhibits mTORC1 signaling in clear cell renal cell carcinoma, *Sci. Rep.*, 2021, **11**(1), 14827.
61 E.-J. Yun, C.-J. Lin, A. Dang, E. Hernandez, J. Guo, W.-M. Chen, J. Allison, N. Kim, P. Kapur and J. Brugarolas, Downregulation of human DAB2IP gene expression in renal cell carcinoma results in resistance to ionizing radiation, *Clin. Cancer Res.*, 2019, **25**(14), 4542–4551.
62 L. Weng, Y. Wang, J. Zhang, Q. Wu, P. Zhao, Y. Shi, P. Wang and L. Fang, Deciphering the role of CD47 in cancer immunotherapy, *J. Adv. Res.*, 2023, **63**, 129–158.
63 Y. Han, D. Liu and L. Li, PD-1/PD-L1 pathway: current researches in cancer, *Am. J. Cancer Res.*, 2020, **10**(3), 727.
64 K. R. Leite, S. T. Reis, J. P. Junior, M. Zerati, D. d. O. Gomes, L. H. Camara-Lopes and M. Srougi, PD-L1 expression in renal cell carcinoma clear cell type is related to unfavorable prognosis, *Diagn. Pathol.*, 2015, **10**, 1–6.
65 H.-R. Park, S.-E. Kim, B. Keam, H. Chung, S. H. Seok, S. Kim, M. Kim, T. M. Kim, J. Doh and D.-W. Kim, Blockade of CD47 enhances the antitumor effect of macrophages in renal cell carcinoma through trogocytosis, *Sci. Rep.*, 2022, **12**(1), 12546.
66 T. Das, G. Sa, E. Paszkiewicz-Kozik, C. Hilston, L. Molto, P. Rayman, D. Kudo, K. Biswas, R. M. Bukowski and J. H. Finke, Renal cell carcinoma tumors induce T cell apoptosis through receptor-dependent and receptor-independent pathways, *J. Immunol.*, 2008, **180**(7), 4687–4696.
67 D. Kudo, P. Rayman, C. Horton, M. K. Cathcart, R. M. Bukowski, M. Thornton, C. Tannenbaum and J. H. Finke, Gangliosides expressed by the renal cell carcinoma cell line SK-RC-45 are involved in tumor-induced apoptosis of T cells, *Cancer Res.*, 2003, **63**(7), 1676–1683.
68 A. Banerjee, B. Mahata, A. Dhir, T. K. Mandal and K. Biswas, Elevated histone H3 acetylation and loss of the Sp1-HDAC1 complex de-repress the GM2-synthase gene in renal cell carcinoma, *J. Biol. Chem.*, 2019, **294**(3), 1005–1018.
69 C. Xu, H. Wu, Y. Liu, F. Li, R. K. Manne and H.-K. Lin, Protocol for detecting macrophage-mediated cancer cell

phagocytosis in vitro and in vivo, *STAR Protoc.*, 2023, **4**(1), 101940.

70 D. Hazama, Y. Yin, Y. Murata, M. Matsuda, T. Okamoto, D. Tanaka, N. Terasaka, J. Zhao, M. Sakamoto and Y. Kakuchi, Macrocyclic peptide-mediated blockade of the CD47-SIRPα interaction as a potential cancer immunotherapy, *Cell Chem. Biol.*, 2020, **27**(9), 1181–1191.

71 H. Wang, Y. Sun, X. Zhou, C. Chen, L. Jiao, W. Li, S. Gou, Y. Li, J. Du and G. Chen, CD47/SIRPα blocking peptide identification and synergistic effect with irradiation for cancer immunotherapy, *J. Immunother. Cancer*, 2020, **8**(2), e000905.

72 A. Kulkarni, V. Chandrasekar, S. K. Natarajan, A. Ramesh, P. Pandey, J. Nirgud, H. Bhatnagar, D. Ashok, A. K. Ajay and S. Sengupta, A designer self-assembled supramolecule amplifies macrophage immune responses against aggressive cancer, *Nat. Biomed. Eng.*, 2018, **2**(8), 589–599.

73 A. Sinha, R. Kushwaha, K. Molesworth, O. Mychko, N. Makarava and I. V. Baskakov, Phagocytic activities of reactive microglia and astrocytes associated with prion diseases are dysregulated in opposite directions, *Cells*, 2021, **10**(7), 1728.

74 L. Erwig and P. Henson, Clearance of apoptotic cells by phagocytes, *Cell Death Differ.*, 2008, **15**(2), 243–250.

75 I. J. Marques, F. U. Weiss, D. H. Vlecken, C. Nitsche, J. Bakkers, A. K. Lagendijk, L. I. Partecke, C.-D. Heidecke, M. M. Lerch and C. P. Bagowski, Metastatic behaviour of primary human tumours in a zebrafish xenotransplantation model, *BMC Cancer*, 2009, **9**, 1–14.

76 S. Ghosh, P. Gayen, S. Jan, A. V. Kishore, V. Kumar, A. M. Mallick, A. Mukherjee, S. K. Nandi and R. Sinha Roy, Bioinspired non-immunogenic multifunctional sealant for efficient blood clotting and suture-free wound closure, *ACS Biomater. Sci. Eng.*, 2020, **6**(11), 6378–6393.

77 E. L. Wu, X. Cheng, S. Jo, H. Rui, K. C. Song, E. M. Dávila-Contreras, Y. Qi, J. Lee, V. Monje-Galvan and R. M. Venable, *CHARMM–GUI membrane builder toward realistic biological membrane simulations*, Wiley Online Library, 2014.

78 S. Jo, J. B. Lim, J. B. Klauda and W. Im, CHARMM-GUI Membrane Builder for mixed bilayers and its application to yeast membranes, *Biophys. J.*, 2009, **97**(1), 50–58.

79 W. L. Jorgensen, J. Chandrasekhar, J. D. Madura, R. W. Impey and M. L. Klein, Comparison of simple potential functions for simulating liquid water, *J. Chem. Phys.*, 1983, **79**(2), 926–935.

80 J. B. Klauda, R. M. Venable, J. A. Freites, J. W. O'Connor, D. J. Tobias, C. Mondragon-Ramirez, I. Vorobyov, A. D. MacKerell Jr and R. W. Pastor, Update of the CHARMM all-atom additive force field for lipids: validation on six lipid types, *J. Phys. Chem. B*, 2010, **114**(23), 7830–7843.

81 W. H. Press, *Numerical recipes: The art of scientific computing*, Cambridge University Press, 3rd edn, 2007.

82 G. Bussi, D. Donadio and M. Parrinello, Canonical sampling through velocity rescaling, *J. Chem. Phys.*, 2007, **126**(1), 014101.

83 G. J. Martyna, M. L. Klein and M. Tuckerman, Nosé–Hoover chains: The canonical ensemble via continuous dynamics, *J. Chem. Phys.*, 1992, **97**(4), 2635–2643.

84 S. Nosé, A molecular dynamics method for simulations in the canonical ensemble, *Mol. Phys.*, 1984, **52**(2), 255–268.

85 M. Parrinello and A. Rahman, Polymorphic transitions in single crystals: A new molecular dynamics method, *J. Appl. Phys.*, 1981, **52**(12), 7182–7190.

86 U. Essmann, L. Perera, M. L. Berkowitz, T. Darden, H. Lee and L. G. Pedersen, A smooth particle mesh Ewald method, *J. Chem. Phys.*, 1995, **103**(19), 8577–8593.

87 B. Hess, H. Bekker, H. J. Berendsen and J. G. Fraaije, LINCS: a linear constraint solver for molecular simulations, *J. Comput. Chem.*, 1997, **18**(12), 1463–1472.

88 H. J. Berendsen, D. van der Spoel and R. van Drunen, GROMACS: A message-passing parallel molecular dynamics implementation, *Comput. Phys. Commun.*, 1995, **91**(1–3), 43–56.

89 A. B. Gurung, K. Chakraborty, S. Ghosh, S. Jan, P. Gayen, A. Biswas, A. M. Mallick, M. Hembram, A. Tripathi and A. Mukherjee, Nanostructured lipopeptide-based membranomimetics for stabilizing bacteriorhodopsin, *Biomater. Sci.*, 2024, **12**(14), 3582–3599.

90 R. Kumari, R. Kumar, O. S. D. D. Consortium and A. Lynn, g_mmpbsa A GROMACS tool for high-throughput MM-PBSA calculations, *J. Chem. Inf. Model.*, 2014, **54**(7), 1951–1962.

91 T. Shinojima, M. Oya, A. Takayanagi, R. Mizuno, N. Shimizu and M. Murai, Renal cancer cells lacking hypoxia inducible factor (HIF)-1α expression maintain vascular endothelial growth factor expression through HIF-2α, *Carcinogenesis*, 2007, **28**(3), 529–536.

92 A. Biswas, K. Chakraborty, C. Dutta, S. Mukherjee, P. Gayen, S. Jan, A. M. Mallick, D. Bhattacharyya and R. Sinha Roy, Engineered histidine-enriched facial Lipopeptides for enhanced intracellular delivery of functional siRNA to triple negative breast Cancer cells, *ACS Appl. Mater. Interfaces*, 2019, **11**(5), 4719–4736.